

UNIVERSITY OF ZURICH

Electronic and Spatial Structures of Self-Assembled Diamondoid Monolayers

by

Markus Baumgartner

Master-Thesis

Supervised by

Prof. Dr. Jürg Osterwalder

Dr. Matthias Hengsberger

in the

Faculty of Science

Physik-Institut

May 2016

UNIVERSITY OF ZURICH

Abstract

Faculty of Science

Physik-Institut

Master-Thesis

by Markus Baumgartner

Diamondoids represent the extreme size limitations of diamond, which is a fascinating material with its numerous outstanding properties. Diamondoids form the sp^3 companions to sp^2 -bonded carbon materials such as graphene, carbon nanotubes and fullerenes. This thesis presents the results of photoemission experiments on self-assembled adamantane, diamantane, and [121]tetramantane monolayers on noble metal surfaces. The growth of diamondoid monolayer on Ag(111) and Au(111) was established. Using various photoemission spectroscopy techniques the electronic and structural properties of diamondoid monolayer and their evolution with increasing diamondoid size was studied.

Acknowledgements

At this point I want to thank several people who made this thesis possible. First of all I want to thank Prof. Jürg Osterwalder and Dr. Matthias Hengsberger who made it possible to write this thesis in the Surface Physics Group. A special thanks go to Adrian Schuler, Dr. Dominik Leuenberger and Wolf Zabka who were always willing to support my work with their experimental knowledge. Many thanks to the other members of the Surface Physics Group sacrificing some time to support my work. Heartfelt thanks to Nina, my family and friends for the everlasting support. I would not be where and who I am without you.

Contents

Abstract	iii
Acknowledgements	iv
1 Introduction	1
1.1 Diamondoids	1
1.2 Negative Electron Affinity	2
1.3 Aims of this Work	3
2 Experimental Methods	5
2.1 Theory of Photoemission	5
2.2 X-ray Photoelectron Spectroscopy and Diffraction	6
2.3 Two Photon Photoemission (2PPE)	7
2.4 Nonlinear Optics	9
3 Experimental Setup	11
3.1 Laser system	11
3.2 Optical Parametric Amplifier (OPA)	12
3.3 Electron Spectrometer	13
4 Photoemission Experiments	15
4.1 Sample and Preparation	15
4.1.1 Substrate preparation	15
4.1.2 Preparation	15
4.2 X-ray Photoelectron Spectroscopy	16
4.2.1 X-ray Photoelectron Spectra	16
4.2.2 Coverage	19
4.3 Spatial Structure	22
4.3.1 X-ray Photoelectron Diffraction Experiments	22
4.4 Electronic Structure	26
4.4.1 Ultraviolet Photoemission Experiments	26
4.4.2 Two-Photon Photoemission Experiments	29
4.4.3 Work function and HOMO-LUMO Gap	37
5 Conclusion	41

Bibliography

Chapter 1

Introduction

1.1 Diamondoids

Diamondoids are small molecules with a typical diameter of about 1 nm. They are formed by carbon and hydrogen atoms in a cage-like structure similar to diamond with sp^3 -type chemical bonds. Clay et al. provide a comprehensive summary of their physical properties [1]. Adamantane, the smallest representative of the family with one cage, is formed by 10 carbon and 16 hydrogen atoms. Other diamondoids are formed by face-fusing a multiplet of such cages together. Diamondoids can be divided into two groups, so-called lower and higher diamondoids, containing one to three or four and more cages respectively. Worth noting is that lower diamondoids only have one geometrical isomer while for higher diamondoids several geometrical isomers exist. The structure of a number of diamondoids is shown in Fig. 1.1. Adamantane was theoretically proposed in 1924 and first isolated from crude oil 1933 in Czechoslovakia [2]. The synthesis of lower diamondoids like adamantane, diamantane and trimantane was realised between 1941 (adamantane) and 1966 (trimantane). All attempts to synthesize higher diamondoids failed so far. With the discovery and extraction of larger quantities of natural diamondoid stocks in petroleum 2003 by Dahl et al. [3], higher diamondoids became available in significant amounts.

Diamondoids possess some of the superior properties of bulk diamond and diamond surfaces as well as properties related to their nanoscale size. For example diamondoid monolayer films lead to monochromatic electron emission due to the attribute of negative electron affinity [4].

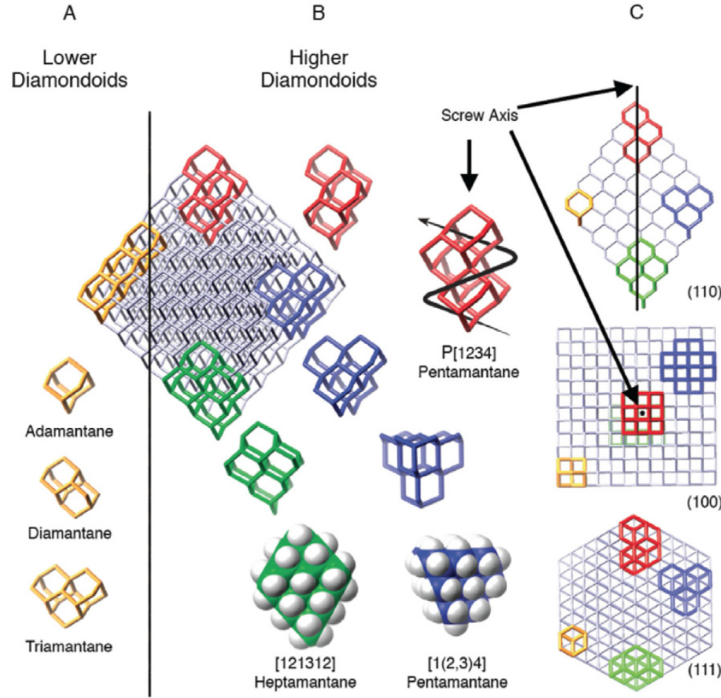


FIGURE 1.1: Structure of a number of diamondoid molecules of different sizes. The three lower diamondoids are shown in the left most column (yellow). On the right hand side the carbon bonding structure and space filling models of higher diamondoids are illustrated. Also shown is the overlay of these structures with the bulk diamond lattice. For clarity surface hydrogens are not shown on the carbon framework structures. Taken from Ref. [3].

1.2 Negative Electron Affinity

The energy difference between the ground state of an atom E_{gs} and the ground state of its negatively charged ion E_{gs}^- is defined as electron affinity.

$$E_{EA} = E_{gs} - E_{gs}^- \quad (1.1)$$

In a solid the electron affinity is defined as the energy difference of the vacuum level E_{vac} at large distance and the conduction band minimum E_{cbm} [5]. The electron affinity is positive for $E_{vac} > E_{cbm}$. For a molecular ad-layer on a metal surface the lowest unoccupied molecular orbital (LUMO) takes the role of the conduction band. Figure 1.2 illustrates this case. If the LUMO is located between E_F and E_{vac} an electron added from infinity to the system will release the energy E_{EA} . In the case were the LUMO is above E_{vac} the electron affinity becomes negative and since the electron lies above E_{vac} it will emit spontaneously into vacuum without requiring additional energy. Negative electron affinity has been observed from diamondoid monolayers [4], a doped diamond(111) surface [5] or cesiated GaAs [6].

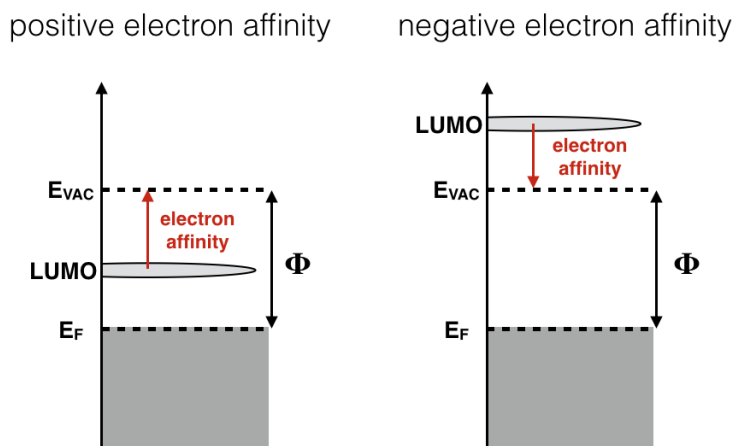


FIGURE 1.2: Energy diagram of a molecular ad-layer on a metal substrate. The red arrow indicates the electron affinity $E_{EA} = E_{vac} - E_{LUMO}$. **Left hand side:** The LUMO is located between E_F and E_{vac} , $E_{EA} > 0$. **Right hand side:** The $E_{LUMO} > E_{vac}$ therefore $E_{EA} < 0$.

1.3 Aims of this Work

The study of diamondoids is attractive for multiple reasons. Firstly, they represent the extreme size limitation for diamond, which is a fascinating material with its numerous outstanding properties like high hardness, excellent thermal stability in absence of oxygen, high heat conductivity and negative electron affinity. Secondly, they form diamond like sp^3 companions to sp^2 -bonded carbon materials such as graphene, carbon nanotubes, and fullerenes. Carbon materials are at the forefront of material science. Understanding the electronic and structural properties of diamondoids and their evolution with increasing size will help in future scientific and commercial applications. Figure 1.3 illustrates the different thiolated diamondoids. This work focuses on the negative electron affinity of self assembled monolayers and the molecular orientation of adamantanethiol (1), diamantane-4-thiol (3), and [121]tetramantane-6-thiol (8) on noble metal surfaces.

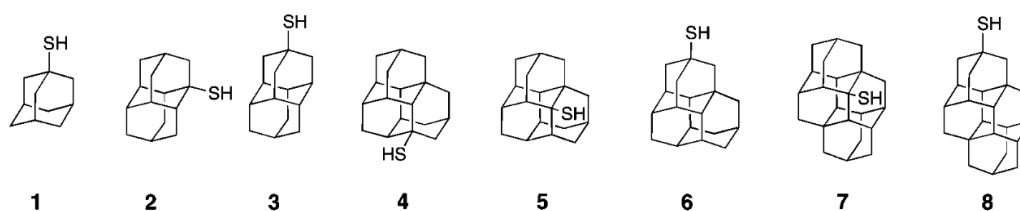


FIGURE 1.3: Illustration of diamondoids with attached thiol-groups. **1**, adamantanethiol; **2**, diamantane-1-thiol; **3**, diamantane-4-thiol; **4**, triamantane-3-thiol; **5**, triamantane-2-thiol; **6**, triamantane-9-thiol; **7**, [121]tetramantane-2-thiol; and **8**, [121]tetramantane-6-thiol. Taken from Ref. [7].

Chapter 2

Experimental Methods

2.1 Theory of Photoemission

Photoelectron spectroscopy is an important tool to study the electronic properties of materials. The information about the electronic structure is obtained by measuring the kinetic energy and the angle of emission of photo emitted electrons. The upper limit for the energy of electrons in a solid in the ground state is called the chemical potential μ which at temperature $T=0$ is called the Fermi energy E_F . Figure 2.1 shows a photoemission process. The binding energy E_B of an electronic state $|i\rangle$ can be defined as:

$$E_B = E_F - E_{|i\rangle} \quad (2.1)$$

The emission of photo electrons out of state $|i\rangle$ occurs when the energy of the incoming photon $h\nu$ is greater than the sum of the work function Φ and the binding energy. Einstein's formula relates the kinetic energy of the emitted electron in vacuum to the photon energy, the work function and the binding energy [8].

$$E_{kin} = h\nu - \Phi - E_B \quad (2.2)$$

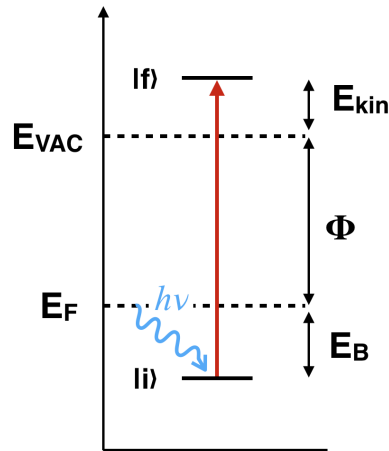


FIGURE 2.1: Photoemission process, the electron is excited from the ground state $|i\rangle$ with binding energy E_B to the final state $|f\rangle$ by absorption of a photon of energy $h\nu$. The final state is detected with a kinetic energy E_{kin} above the vacuum energy E_{vac} . The work function Φ is the difference between E_{vac} and E_F .

2.2 X-ray Photoelectron Spectroscopy and Diffraction

X-ray photoelectron spectroscopy (XPS) uses the photoelectric effect, described in section 2.1, to study the binding energies of the deep lying core-levels inside a sample. Due to the shallow depth of a few atomic layers from which elastically scattered electrons are detected, it is an ideal tool to study thin films and surfaces. First developed by Siegbahn in 1967 it is also known as ESCA (electron spectroscopy for chemical analysis) [9]. With the knowledge of photoemission cross section, core-level energies, and chemical shifts the quantitative analysis of XPS spectra and thereby, the determination of the chemical composition of the sample are straight forward.

Using x-ray photoelectron diffraction (XPD) it is further possible to study the atomic positions on the surface [10]. The source of electrons emitted from core levels are well localized at the atomic positions of the specific element. The outgoing photo electron waves are scattered by neighboring atoms. The amplitudes of scattered and direct wave add up coherently forming an angular intensity distribution, the diffraction pattern. Figure 2.2 illustrates the scattering process used by XPD. In the case that all emitter atoms have the same atomic environment a well-defined pattern is recorded from the sample. These diffraction patterns carry a wealth of information about the environment of the emitting atoms. Since core-level peaks are specific for each element the XPD pattern holds information about the short range order around a certain atomic species. Most XPD experiments are performed in a kinetic energy range above 500 eV where the absolute magnitude of the angle dependent scattering amplitude $|f(\Theta)|$ is largest for small Θ . This forward scattering enhancement is called forward focusing [11].

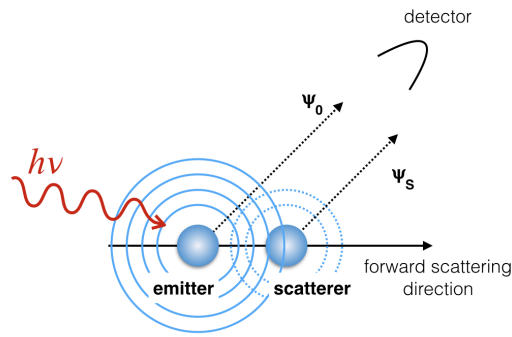


FIGURE 2.2: X-ray photoelectron diffraction. A photon impinging on an atom (emitter) excites a photoelectron which can be approximated as a wave with a spherical wavefront. This spherical wave is scattered by neighboring atoms. The intensity measured at the detector is $I \propto |\Psi_0 + \Psi_S|^2$.

For an example of $|f(\Theta)|$ for two different kinetic energies see Figure 2.3. In this case the angular distribution of the photoelectrons is up to a first approximation the forward projected atomic structure around the emitting atoms.

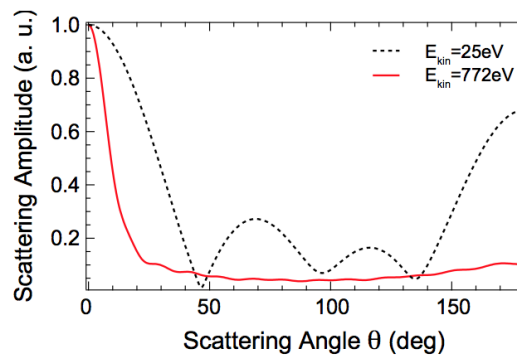


FIGURE 2.3: Scattering amplitude of electrons in silver calculated with in the plane wave approximation. $|f(\Theta)|$ is shown for $E_{kin} = 772$ eV (red) and $E_{kin} = 25$ eV (dashed black). Taken from Ref. [12].

2.3 Two Photon Photoemission (2PPE)

In Section 2.1 we stated that photoemission occurs if $h\nu > \Phi$, and we assumed that each electron absorbs only a single photon. If the photon density is high enough multi-photon processes become possible. This gives a new constraint on the photon energy.

$$n \cdot h\nu > \Phi \quad n \in \mathbb{N} \quad (2.3)$$

Figure 2.4 shows a schematic two-photon photoemission process. An electron is emitted into vacuum $|f\rangle$ via an intermediate state $|m\rangle$. Figure 2.5 depicts the two other main

types of emission processes. (i) Shows a excitation via a virtual intermediate state. (ii) shows an interband excitation where the indirect transition is mediated by a phonon. The electron gains (loses) momentum by absorbing (emitting) a phonon.

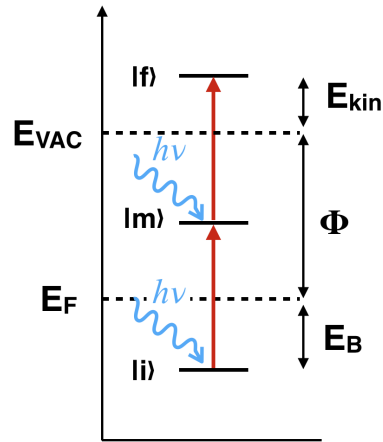


FIGURE 2.4: Illustration of a 2PPE process. The electron is excited by a first photon into an intermediate state $|m\rangle$. A second photon excites the electron from $|m\rangle$ into the final state $|f\rangle$.

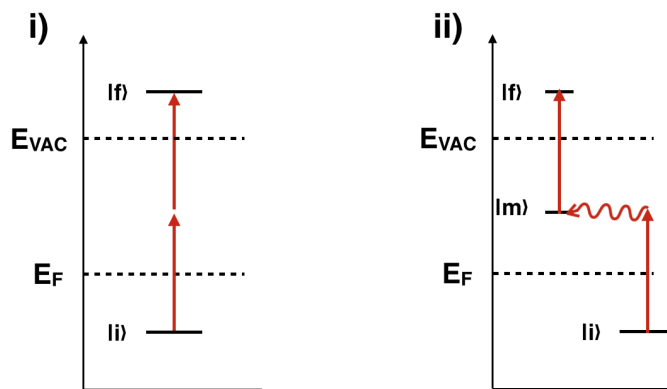


FIGURE 2.5: An example band structure along the $\bar{\Gamma L}$ line. Three possible types of 2PPE processes are shown. **i)** Two-photon excitation by a virtual intermediate state. **ii)** Phonon mediated interband excitation. A first photon excites the electron into a virtual intermediate state, there it absorbs or emits a phonon and relaxes into a real intermediate state by gaining or losing momentum. The energy is almost unchanged. A second photon excites the electron into vacuum.

By observing the evolution of the kinetic energy of the final state $|f\rangle$ with changing photon energy $h\nu$ one can distinguish the nature of the involved states. A shift with twice the photon energy indicates that the initial state remains the same and that the intermediate state is also shifting with once the photon energy. If the kinetic energy of the final state shifts with once the photon energy the intermediate state remains the same. If E_{kin} remains constant the final state is the same for all energies. This is the case

for negative electron affinity where electrons are emitted via the LUMO of the molecule, resulting in the same kinetic energy independent of the excitation energy.

2.4 Nonlinear Optics

When perturbed by an external electromagnetic field positive and negative charges inside a material are displaced. The sum of the induced dipole moments is called the polarization. The electric susceptibility χ is defined as

$$\mathbf{P} = \epsilon_0 \chi \mathbf{E} \quad (2.4)$$

where \mathbf{P} is the macroscopic polarization of a medium when it is illuminated by an external electric field \mathbf{E} . For high field strength higher order terms become important. The equation 2.4 can be expanded in a Taylor-series:

$$\mathbf{P} = \epsilon_0 (\chi^{(1)} \mathbf{E} + \chi^{(2)} \mathbf{E}^2 + \chi^{(3)} \mathbf{E}^3 + \dots) \quad (2.5)$$

where the linear first-order term in the electric field describes linear optics, refractive index and absorption, the second-order term accounts for second order optical effects like second-harmonic generation (SHG) and parametric interactions. The cubic third-order term describes processes like third-harmonic generation.

For the idealized case that the external electromagnetic field strength consists of a pure sine wave

$$\mathbf{E} = \mathbf{E}_0 \sin \omega t, \quad (2.6)$$

the polarization up to the second order is equal to

$$\mathbf{P} = \epsilon_0 (\chi^{(1)} \mathbf{E}_0 \sin \omega t + \chi^{(2)} \mathbf{E}_0 \sin^2 \omega t). \quad (2.7)$$

Using simple trigonometry this can be written as:

$$\mathbf{P} = \frac{\epsilon_0}{2} \chi^{(2)} \mathbf{E}_0^2 + \epsilon_0 \chi^{(1)} \mathbf{E}_0 \sin \omega t - \frac{\epsilon_0 \chi^{(2)}}{2} \mathbf{E}_0^2 \cos 2\omega t \quad (2.8)$$

$$\mathbf{P} = \mathbf{P}_0(0) + \mathbf{P}_L(\omega) + \mathbf{P}_{NL}(2\omega) \quad (2.9)$$

The polarization will emit an electromagnetic field with frequencies ω and 2ω . The polarization travels inside the medium with the same speed as the electric field which caused it $c_1 = c_0/\eta(\omega)$. The electric field emitted by $\mathbf{P}_{NL}(2\omega)$ travels with the speed

$c_2 = c_0/\eta(\omega)$. To obtain constructive interference and to get intense light of frequency 2ω the following relation between c_1 and c_2 has to hold:

$$c_1(\omega) = c_2(2\omega), \quad (2.10)$$

this is equivalent to:

$$\eta_1(\omega) = \eta_2(2\omega) \quad (2.11)$$

the index-matching condition.

This is also equivalent to:

$$1/\lambda_1 = 2/\lambda_2. \quad (2.12)$$

By introducing the wave vector $|\mathbf{k}| = 2\pi/\lambda$ and the momentum of the photon $|\mathbf{p}| = h/\lambda$ the index matching condition is equivalent to the momentum conservation:

$$\mathbf{p}_2 = \mathbf{p}_1 + \mathbf{p}_1. \quad (2.13)$$

In order to fulfill the index-matching condition one uses birefringent crystals. If two intense light waves of frequencies ω_1 and ω_2 impinge on such a crystal not only the second harmonics $2\omega_1$ and $2\omega_2$ are emitted, equation 2.5 allows for the generation of the difference frequency $\omega_1 - \omega_2$ and the sum frequency $\omega_1 + \omega_2$, if the refractive indices were matched.

This effect can be used to amplify light of ω_{sig} by pumping the crystal with light of frequency ω_{pump} . Due to energy conservation an idler frequency ω_i has to be produced

$$\omega_i = \omega_{pump} - \omega_{sig}. \quad (2.14)$$

The amplification then is described by:

$$\omega_{pump} + \omega_{sig} = 2\omega_{sig} + \omega_{idler} \quad (2.15)$$

For a more in-depth look the reader is referred to a text book about optics, for example [13].

Chapter 3

Experimental Setup

3.1 Laser system

As stated in Section 2.3 multi-photon photoemission occurs if the photon density is high. Pulsed laser systems provide such high peak intensities. The 2PPE experiments in this thesis were performed using a femtosecond laser system manufactured by Coherent Inc., which will be described in detail.

The oscillator, a Mira Seed, is a passively mode-locked Kerr-lense Ti:sapphire oscillator which is pumped by a 5 W Verdi-V5 Nd:Vanadate diode-pumped solid state laser. In continuous wave mode an average output power of >1 W, in pulsed mode >500 mW is achieved. The wavelength can be varied between 780 nm to 840 nm, the spectral width of $\Delta\lambda = 30$ nm results in a pulse duration of ~ 50 fs behind the output coupler. With a repetition rate of $\nu_{rep} = 76$ MHz a pulse energy of 6.6 nJ can be achieved.

In order to amplify the pulse power a regenerative amplifier (RegA) is used. The RegA 9050 is a high repetition rate regenerative Ti:sapphire amplifier with a tunable repetition rate from 100 kHz to 300 kHz. To pump the RegA a Verdi-V10 10 W continuous wave Nd:Vanadate solid state laser is used. The output power of the RegA reaches up to 1.2 W at a repetition rate of 250 kHz and a pulse energy of 4.8 μ J respectively 0.65 W at a repetition rate of 100 kHz and an energy of 6.5 μ J per pulse. An EC9100 grating compressor/expander unit is used to stretch (compress) the incoming (outgoing) pulses of the amplifier. The output of the compressor usually has a pulse duration as short as $\Delta t = 56$ fs.

Femtosecond pulses over a wide wavelength range are produced in an optical parametric amplifier (OPA). Out of a white light continuum a specific wavelength can be chosen to be amplified. The OPA 9450 can amplify pulses between 470 nm to 720 nm. Beside the signal output (470 nm to 720 nm) the OPA provides the remaining pump light (400 nm)

and the idler output which is the difference frequency of the pump and the amplified signal ($\hbar\omega_{idler} = \hbar\omega_{pump} - \hbar\omega_{sig}$).

To produce wavelengths smaller than 400 nm the signal output of the OPA was frequency doubled in a β -Barium Borate crystal (**S**econd **H**armonic **G**eneration (SHG)) before being transferred to the vacuum chamber equipped with a photoelectron spectrometer. For brief explanation of the involved nonlinear optics in the OPA and SHG see Section 2.4.

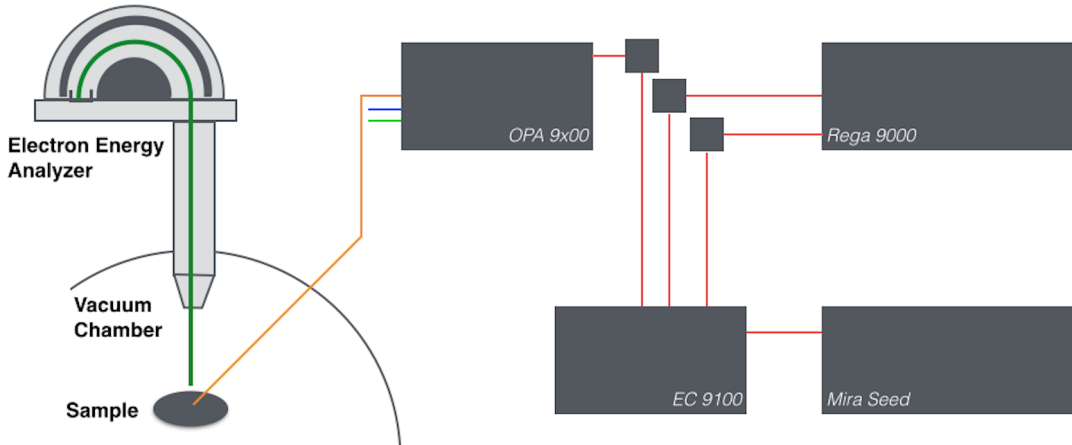


FIGURE 3.1: Sketch of the laser system and the ESCA vacuum chamber. The pulse of the Mira Seed is first going to the grating compressor/expander unit before being amplified in the RegA. After another pass through the compressor the light is entering the OPA. The OPA provides three outputs, a signal pulse with a selectable wavelength (470 nm to 720 nm, the rest of the frequency doubled pump pulse 400 nm and the Idler the difference of the signal and the pump pulse. To access energies above 3.1 eV (400 nm) the signal of the OPA was further frequency doubled in a BBO crystal (not depicted in this figure).

3.2 Optical Parametric Amplifier (OPA)

The optical parametric amplifier uses the RegA output to produce tunable amplified femtosecond output pulses from 470 nm to 700 nm. An OPA optical schematic is shown in Fig. 3.2. The 800 nm RegA output is split by M1. 75 % of the energy goes via M2 into the second harmonic generation (SHG). L1 focuses the beam onto the SHG crystal. The frequency is doubled by the SHG to produce a pump beam at 400 nm. The pump beam is steered by M3 to the dichroic mirror D1 white light.

The remaining 25 % of the RegA output are focused by lens L4 onto a Sapphire crystal (S) to generate a white light continuum. Lens L5 collimates the white light. Before being combined with the pump beam at mirror D1 the white light goes through an adjustable delay (1st pass) consisting of M4 and M5.

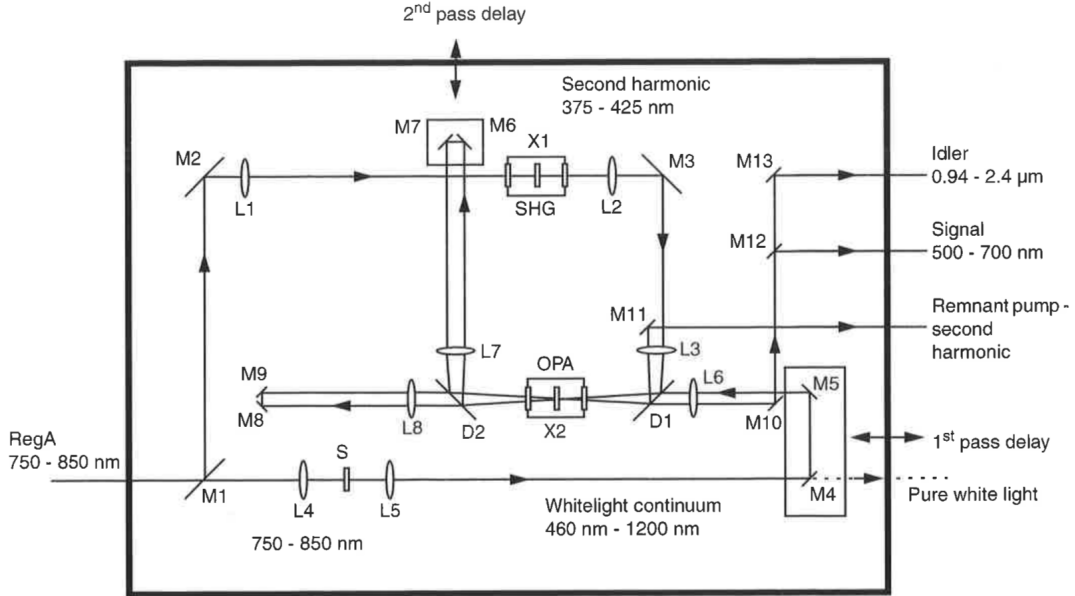


FIGURE 3.2: OPA Optical Schematic taken from [14].

After the first pass through the OPA crystal (BBO), the two beams are separated by D2. The white light passes through a second fixed optical delay (M8 and M9). The pump pulse passes an adjustable delay (2nd pass) consisting of M6 and M7. The two beams are recombined at D2 for a second pass through the OPA. After the second pass the idler, signal and remnant pump beams exit the OPA via the mirrors M11, M12 and M13. The angles of both SHG and OPA crystals as well as the delays can be tuned by external micrometer screws.

3.3 Electron Spectrometer

The VG ESCALab is a multi-chamber vacuum system (base pressure $\approx 5 \cdot 10^{-11}$ mbar). The chambers of the system allow for the preparation of samples under ultrahigh vacuum conditions and analysis of the electronic and atomic structures. The analysis chamber is shown in Figure 3.3. It contains several photon sources. For the XPS and XPD measurements the Mg $K\alpha$ x-ray gun with a photon energy of $h\nu = 1253.6$ eV was used. Ultraviolet spectroscopy was performed with the He discharge lamp providing photon energies of $h\nu = 21.2$ eV (He I α) and $h\nu = 40.8$ eV (He II α). Externally generated laser light can be brought into the chamber via a viewport with an angle of incidence of 30° with respect to the energy analyzer. To increase the kinetic energy of the emitted electrons a bias voltage can be applied to the sample. The detector has an energy resolution of 20 meV and an angular resolution of 1° . More information about the system can be found in [15].

All measurements were carried out using the usual settings for the electron optics. For the UPS and 2PPE measurements a bias voltage of -10 V between sample and ground generated with a power supply was applied. The focus of the laser light was chosen to optimize to maximize the intensity on the sample with minimal space charge effects.

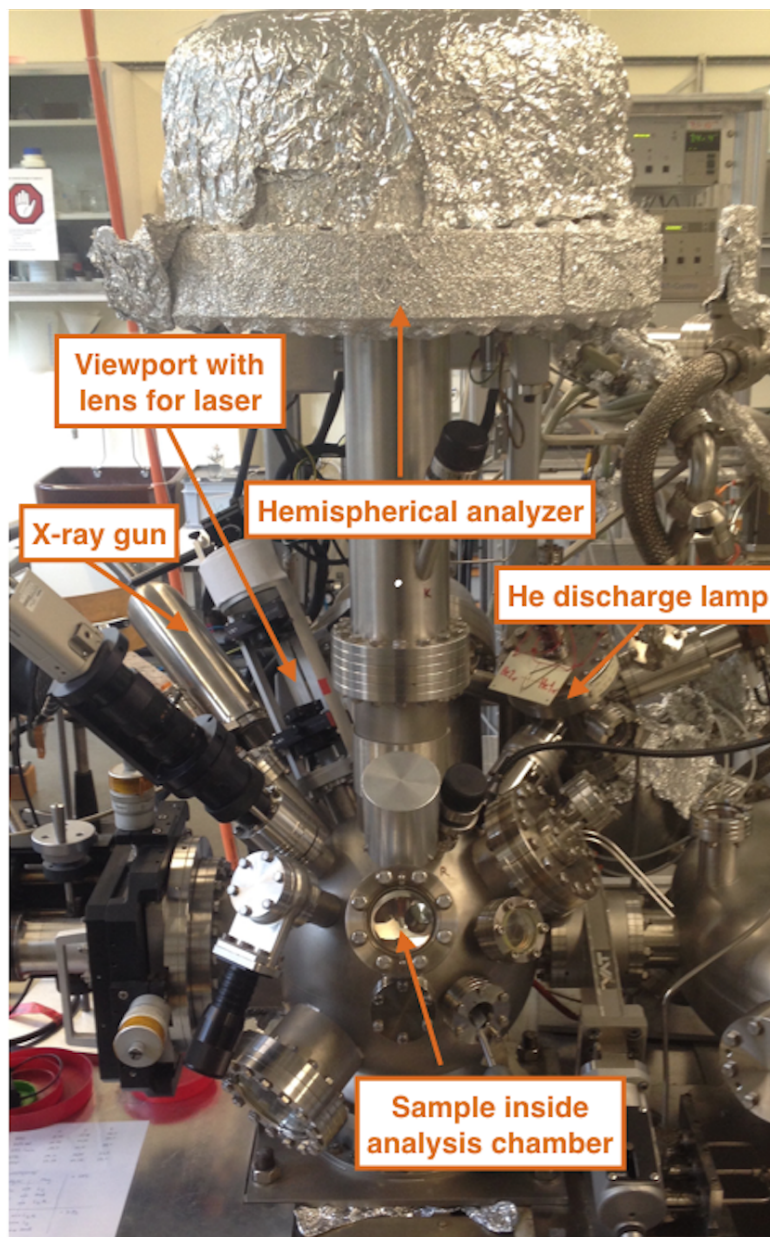


FIGURE 3.3: The ESCA chamber. The hemispherical analyzer is mounted on top. On the left hand side of the chamber the x-ray gun is mounted. Next to it one can see the viewport with the lens for the laser. On the right hand side the He-discharge lamp with a monochromator is mounted to the chamber. Inside the chamber the sample is mounted on a manipulator allowing for translations in x,y,z as well as rotations of polar and azimuthal angle.

Chapter 4

Photoemission Experiments

4.1 Sample and Preparation

4.1.1 Substrate preparation

In order to grow the diamondoid monolayers the (111) surfaces of Ag and Au single crystals were used. The substrates were cleaned by Ar sputtering. To accelerate the Ar-Ions further an additional discharge potential of 0.75 kV was used for the first cycle which was decreased in consecutive cleaning cycles to 0.5 kV and 0 kV for silver. In the case of the gold substrate a discharge potential of 0.6 kV was applied for all cycles. After sputtering for 15 min for silver and initially for 30 min, then for 20 min for gold, the samples were annealed by increasing the heating current stepwise allowing for a maximal pressure of $3 \cdot 10^{-8}$ mbar. The sample was annealed for 15 min at 420 °C for silver and 490 °C in the case of gold. These cycles were repeated two to four times to retrieve a clean surface. During the last cleaning cycle the pressure never exceeded $8 \cdot 10^{-9}$ mbar. XPS and UPS spectra of the clean substrates can be found in Section 4.2.1.

4.1.2 Preparation

To prepare self-assembled monolayers (SAM) of diamondoids on noble metal substrates the thiolated diamondoids are deposited from solution. To allow the formation of a self-assembled monolayer the substrate surface is submerged in a solution of 90 % ethanol and 10 % toluene with a concentration of 0.1 to 10 mmol L⁻¹ of diamondoids for at least 24 h [16]. For the preparations in this work concentrations from 2 to 6 mmol L⁻¹ were used and the exposure time ranged from 37 to 66 hours. Figure 4.1 shows the Au(111) substrate inside the V-shaped glass vial submerged in the solution. After deposition

of the diamondoids the sample was washed with toluene and ethanol and immediately inserted in the ultra high vacuum.



FIGURE 4.1: Photo of the Au[111] substrate inside the V-shaped glass vial. The surface is completely immersed in the diamondoid solution. On the right hand side a small air pocket is visible which grazes the side of the substrate.

4.2 X-ray Photoelectron Spectroscopy

4.2.1 X-ray Photoelectron Spectra

In Figure 4.2 and 4.3 x-ray photoelectron spectra of the Ag(111) and Au(111) surfaces can be found. The surfaces were cleaned as described in Section 4.1.1. Typical impurities like carbon or oxygen are not observed for the clean substrate. The Figures 4.4 and 4.5 show survey spectra of the substrates after deposition of diamondoid-thiols from solution. Both show an increased intensity at the C 1s and S 2p binding energies resulting from the deposited diamondoid layer. Detailed XP-spectra of the Ag 3d, the Au4f respectively and the C 1s and S 2p core level peaks are shown in Figure 4.6. The S 2p_{3/2} binding energy is shifted from 164 eV for atomic sulfur to 162 eV which is characteristic for a metal-thiol bond [17]. Note that the spin-orbit-splitting of the S 2p_{3/2} and S 2p_{1/2} states ($\Delta = 1.18$ eV) could not be resolved. The increase in O 1s signal can be explained by the short exposure to air and oxygen impurities in the solvent.

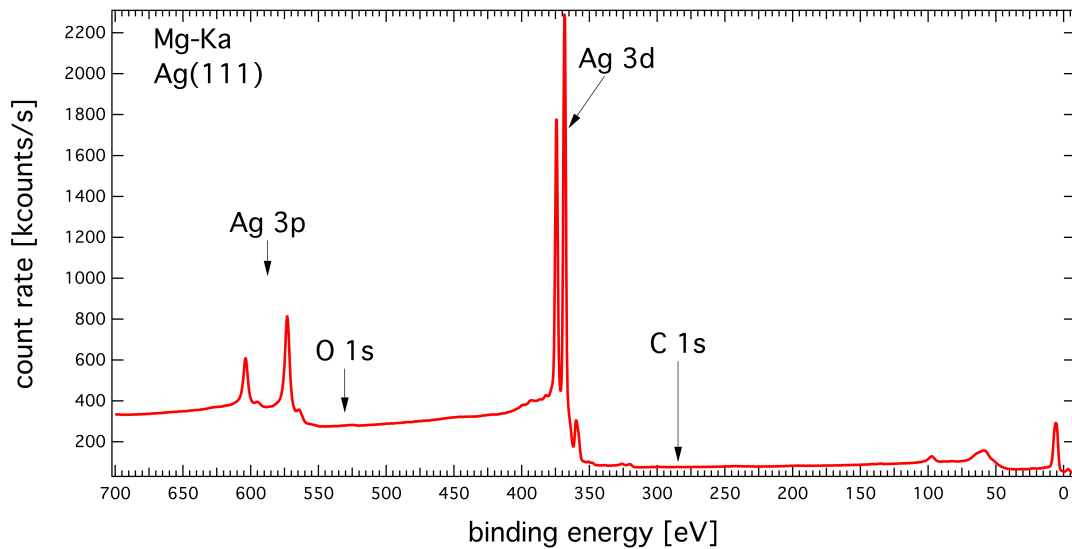


FIGURE 4.2: A x-ray photoemission spectrum of the clean silver substrate in normal emission shown as function of binding energy. The $\text{MgK}\alpha$ source ($h\nu = 1253.6 \text{ eV}$) was used. The $\text{Ag } 3d_{5/2,3/2}$ core states are represented by the two strong peaks at 368 eV binding energy. The two less prominent $\text{Ag } 3p_{3/2,1/2}$ peaks can be seen at 573 eV and 604 eV, respectively. No signal is visible at the C 1s (285 eV) and O 1s (531 eV) binding energies.

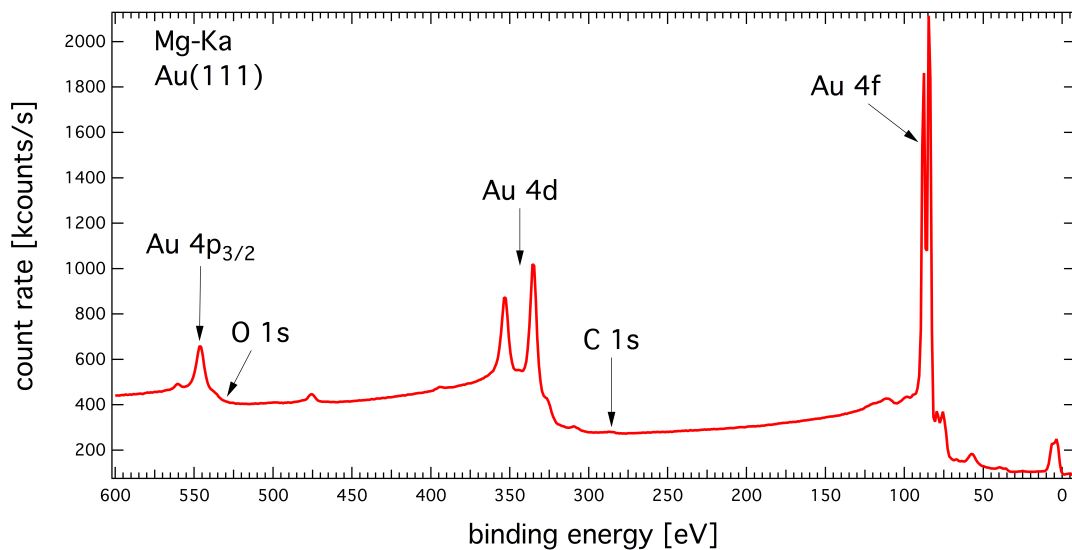


FIGURE 4.3: As in Fig. 4.2: XPS from a clean Au(111) surface. The two strong peaks of the $\text{Au } 4f_{7/2,5/2}$ core states are visible at 84.0 eV and 87.6 eV binding energies. The smaller $\text{Au } 4d_{5/2,3/2}$ peaks are represented at a binding energy of 335.1 eV and 353.2 eV respectively. The $\text{Au } 4p_{3/2}$ core state with a binding energy of 546.3 eV can be seen on the far left of the spectrum. There is no signal visible at binding energies of the typical impurities the C 1s (285 eV) and O 1s (531 eV).

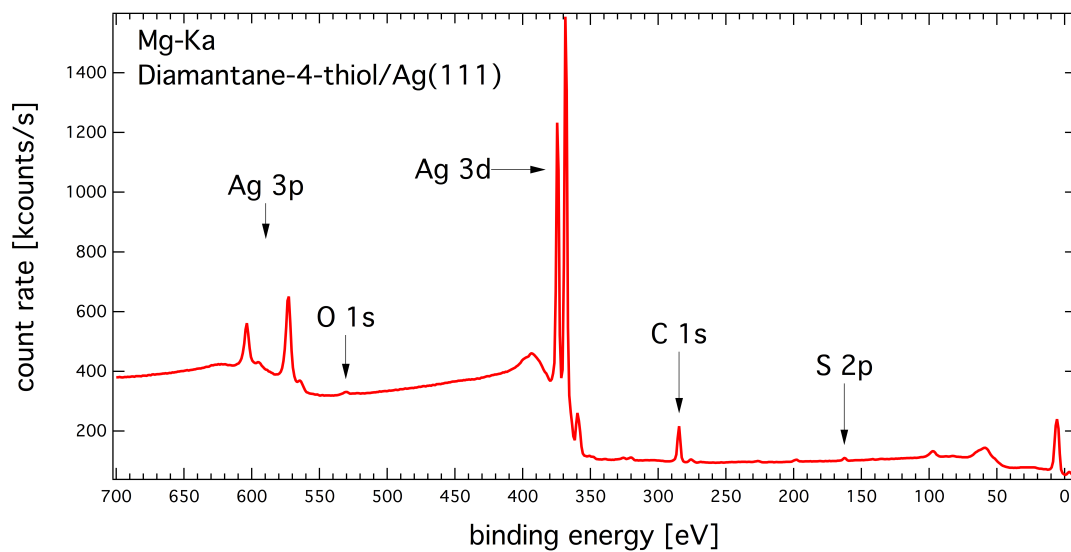


FIGURE 4.4: As in Fig. 4.2: XPS from a diamantane monolayer on Ag(111). In comparison with the clean silver spectrum in Fig. 4.2 a strong peak at the binding energy of C 1s (285 eV) is observed. The signal is also slightly increased at the binding energy of 162 eV which corresponds to the S 2p_{3/2} core level. The increase at the C 1s and S 2p binding energies result from the diamantane ad-layer.

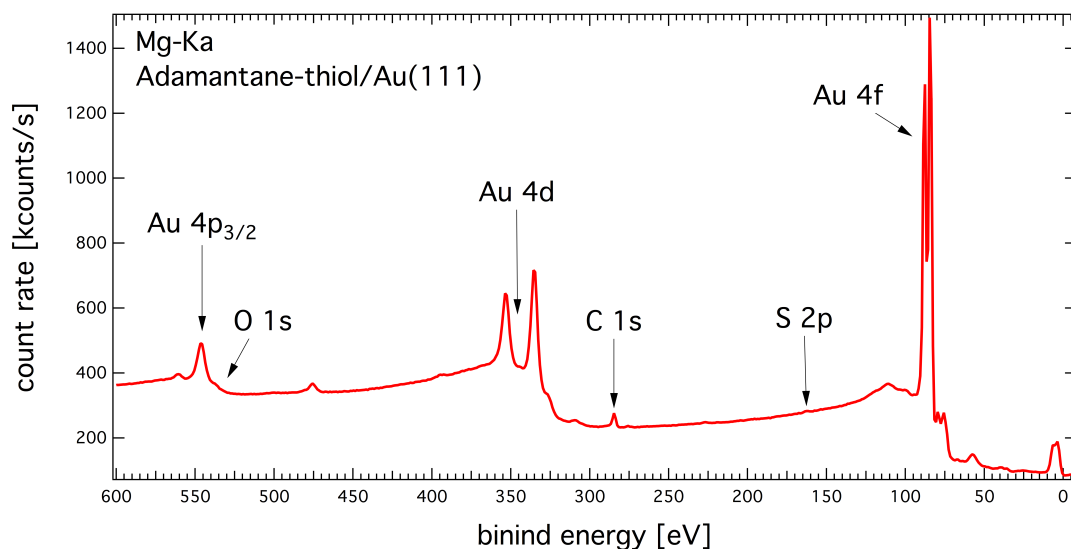


FIGURE 4.5: As in Fig. 4.4: XPS from an adamantane monolayer on Au(111).

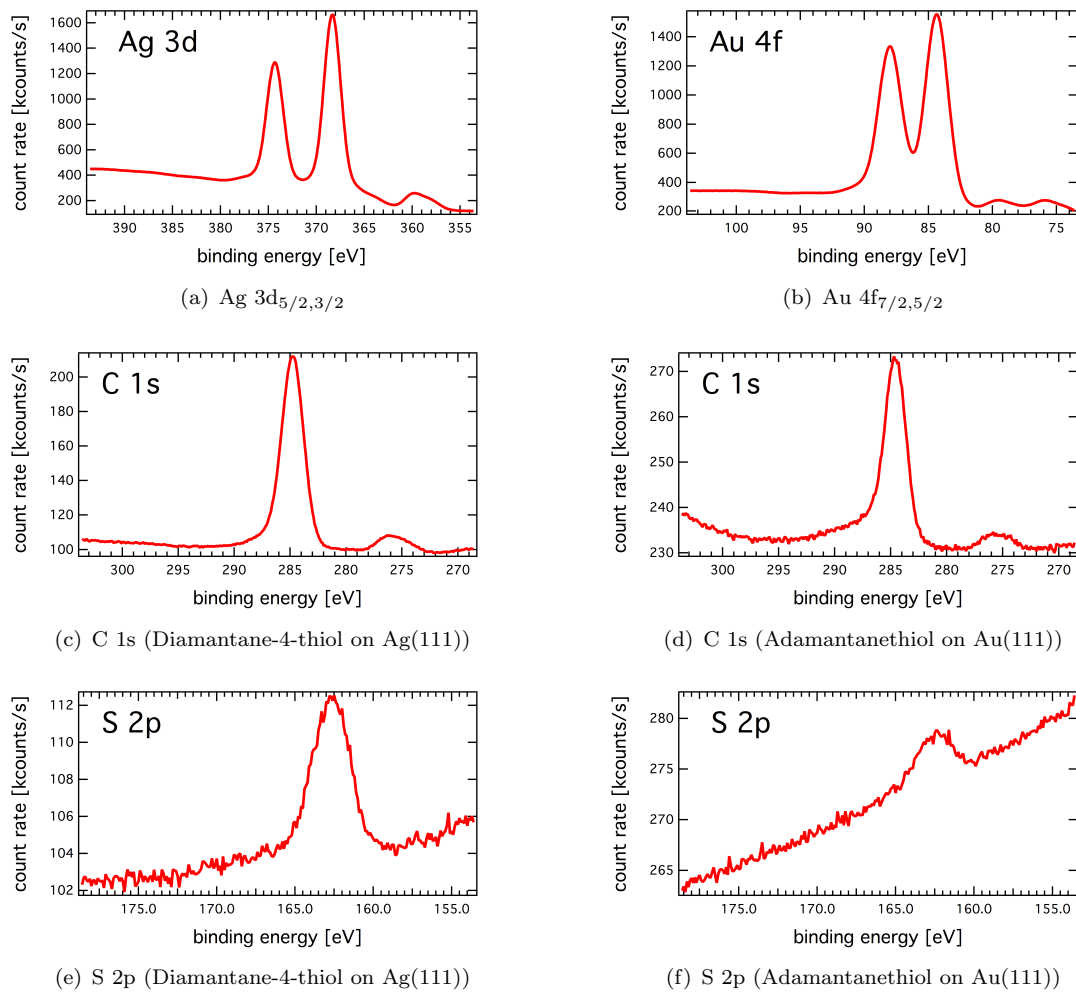


FIGURE 4.6: Detailed x-ray photoemission spectra. In the left column the Ag 3d, C 1s and S 2p core level states from diamantane layer on Ag(111) are shown. In the right column the Au 4f, C 1s and S 2p spectra of a adamantane layer on Au(111) are listed. All spectra are shown as function of binding energy and a photon energy of $h\nu = 1253.6$ eV was used. **(a)** Ag 3d peaks: The binding energy of the Ag 3d_{5/2} is at 368.3 eV. **(b)** Au 4f peaks: The binding energy of the Au 4f_{7/2} is at 84.3 eV. **(c) and (d)** C 1s peak: The binding energy is in good agreement with the value given for carbon (284 eV to 285 eV). **(e) and (f)** S 2p peaks: The binding energy for the S 2p_{3/2} peak is 162 eV. This indicates a metal-thiol bond [17].

4.2.2 Coverage

In order to calculate the coverage of the substrate by diamondoid molecules a simple model was used. In general the following relation for the photoelectron intensity holds:

$$I \sim n \cdot \sigma \cdot \lambda \cdot A \cdot J_{h\nu} \quad (4.1)$$

Here n is the number density of the atom in the observed volume, σ is the cross section of the observed core electron, λ is the inelastic mean free path, A is the observed area

of the sample and $J_{h\nu}$ is the flux of the light source [10].

Since the coverage of the substrate is not known there are two contributions for the intensity from the substrate. The first part is the signal which is not going through a molecule layer on top of the substrate. Figure 4.7 shows the situation for a not completed monolayer of diamondoids.

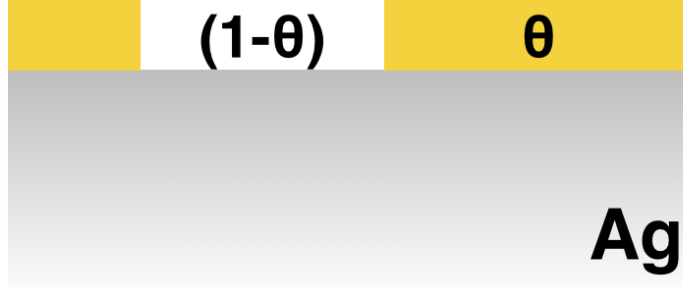


FIGURE 4.7: Coverage model, the substrate is covered by a molecule layer Θ . The part which is not covered is $(1 - \Theta)$.

$$I \sim n_{Sub} \cdot \sigma_{Sub} \cdot \lambda_{Sub} \cdot A \cdot J_{h\nu} \cdot (1 - \theta) \quad (4.2)$$

The second contribution is attenuated by the molecule layer:

$$I \sim n_{Sub} \cdot \sigma_{Sub} \cdot \lambda_{Sub} \cdot A \cdot J_{h\nu} \cdot \theta \cdot e^{-\frac{d_m}{\lambda_m}} \quad (4.3)$$

The sum of both contributions gives the total intensity from the substrate:

$$I \sim n_{Sub} \cdot \sigma_{Sub} \cdot \lambda_{Sub} \cdot A \cdot J_{h\nu} \cdot \left[(1 - \theta) + \theta \cdot e^{-\frac{d_m}{\lambda_m}} \right] \quad (4.4)$$

For the signal of the diamondoid SAM one has to take into account the attenuation by the molecule itself. We are using the S 2p signal of the molecules for this calculation. The sulfur atom sits at the bottom of the molecule and is the atom binding to the substrate. Therefore the signal from the sulfur should be attenuated by the carbon cages lying above.

$$I \sim n_m \cdot \sigma_{S2p} \cdot \lambda_m \cdot A \cdot J_{h\nu} \cdot \theta \cdot e^{-\frac{d_m}{\lambda_m}} \quad (4.5)$$

We find the following expression for the ratio of the intensities:

$$\frac{I_{S2p}}{I_{Sub}} = \frac{n_m \cdot \sigma_{S2p} \cdot \lambda_m \cdot A \cdot J_{h\nu} \cdot \theta \cdot e^{-\frac{d_m}{\lambda_m}}}{n_{Sub} \cdot \sigma_{Sub} \cdot \lambda_{Sub} \cdot A \cdot J_{h\nu} \cdot \left[(1 - \theta) + \theta \cdot e^{-\frac{d_m}{\lambda_m}} \right]} \quad (4.6)$$

One can express the ratio of the number densities via the area density and the thickness of the atom layer. R is the ratio of the area number density of the substrate and the molecule, i.e. the ratio of surface atoms to molecules.

$$\frac{n_m}{n_{Sub}} = \frac{d_{Sub}}{R \cdot d_m} \quad (4.7)$$

$\frac{\lambda}{d}$ is the number of contributing layers. Since we are dealing with a process terminating it self after one monolayer $\Theta = 1$ and $\frac{\lambda_m}{d_m} = 1$.

$$\frac{I_{S2p}}{I_{Sub}} = \frac{d_{Sub} \cdot \sigma_{S2p}}{R \cdot \sigma_{Sub} \cdot \lambda_{Sub}} \quad (4.8)$$

R can then be calculated as:

$$R = \frac{I_{Sub} \cdot d_{Sub} \cdot \sigma_{S2p}}{I_{S2p} \cdot \lambda_{Sub} \cdot \sigma_{Sub}} \quad (4.9)$$

For all calculations the following values for the different material properties were used: $\lambda_{Ag} = 1.55$ nm, $\lambda_{Au} = 1.55$ nm, $d_{Ag} = 0.2359$ nm, $d_{Au} = 0.2355$ nm

TABLE 4.1: Photoionization cross sections for $h\nu = 1253.6$ eV. Taken from [18].

σ_{S2p}	σ_{Ag3d}	σ_{Au4f}
0.038 Mb	0.4052 Mb	0.4176 Mb

R , the ratio of surface atoms to molecules, was reported to be 3 for tetramantane on silver [16]. On gold R was calculated to be 5.7 using the unit cell density reported in [19]. These values were used for comparing adamantane, diamantane and tetramantane since the unit cell density of these species on gold are within the error bars equal [19].

Table 4.2 lists the measured R for preparations of adamantane-thiol, diamantane-4-thiol and [121]tetramantane-6-thiol on Ag(111) and Au(111). The results for gold are in good agreement with values from the literature. For preparations on silver a decrease in R can be observed corresponding to a increase in area density of the smaller diamondoid molecules.

TABLE 4.2: Ration of surface atoms to molecules R for diamondoids on Ag(111) and Au(111). No preparation was done for tetramantane on gold.

	Ag(111)	Au(111)
adamantane-thiol	2.28 ± 0.20	5.95 ± 0.21
diamantane-4-thiol	2.71 ± 0.20	5.60 ± 0.20
[121]tetramantane-6-thiol	3.08 ± 0.22	—
Literature	3	5.7

4.3 Spatial Structure

4.3.1 X-ray Photoelectron Diffraction Experiments

In order to determine the orientation of the absorbed molecules XPD measurements were carried out. All XPD measurements were performed with MgK_{α} light. The S $2p_{3/2}$ core level state was chosen as emitter. The data were normalized to the channeltron sensitivities before an inelastic background was subtracted. To account for the instrumental polar intensity distribution the data were divided by a Gaussian shaped polar intensity distribution profile. In addition the patterns were three fold averaged. Figure 4.8 illustrates how the inelastic background was calculated using the intercept theorem. Figure 4.9 shows the raw data, the pattern after background subtraction and the final pattern.

Figure 4.10 shows XPD patterns for different self-assembled diamondoid monolayers on Ag(111) (a to c) and on Au(111) (d and e). Using the S $2p$ core level state as emitter. All patterns show ring-like intensity distributions at a polar angle $\Theta \approx 38^{\circ}$, except diamantane-4-thiol on Au(111) (Fig. 4.10 (e)) where a strong ring is visible at $\Theta \approx 53^{\circ}$. We attribute the ring-like structure to forward scattering by the nearest carbon atom which corresponds to the direction of the molecular axis, the thiol bond direction. There seems to be no long range azimuthal ordering. This is the reason why we observe rings in the XPD patterns.

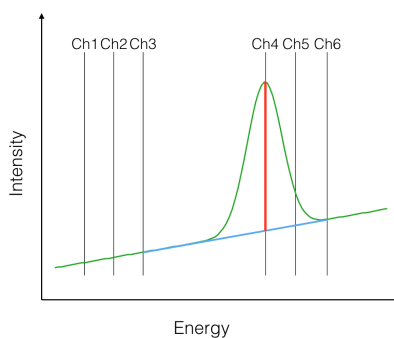


FIGURE 4.8: Illustrations of the background subtraction. Channeltron 4 (Ch4) is set to the energy position of the peak the positions of the other channeltrons are given by the energy analyzer. Assuming a linear background one can use the intercept theorem to calculate the background. In the depicted case Ch3 and Ch6 were used. The background between Ch3 and Ch6 is shown in blue, the resulting signal of Ch4 is shown in red.

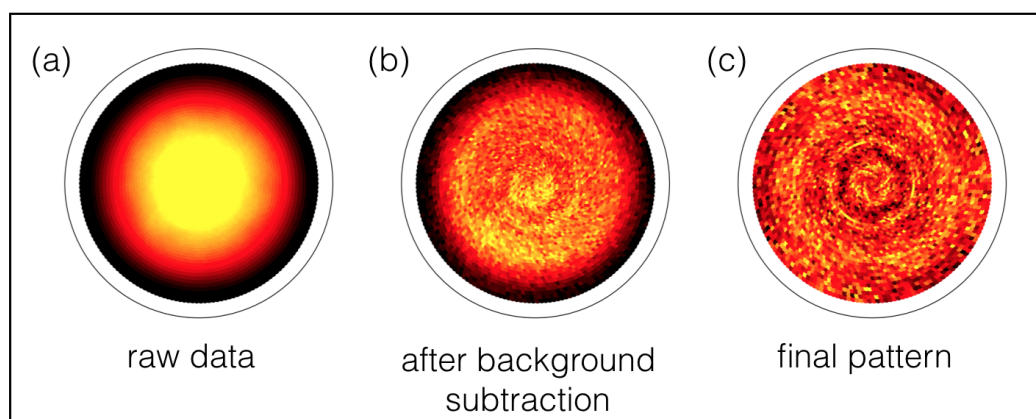


FIGURE 4.9: Data treatment of the XPD pattern for tetramantane on Ag(111) over the process of data analysis. (a) Raw data, (b) after subtraction of the inelastic background and (c) after division by the Gaussian shaped polar background profile and 3-fold averaging.

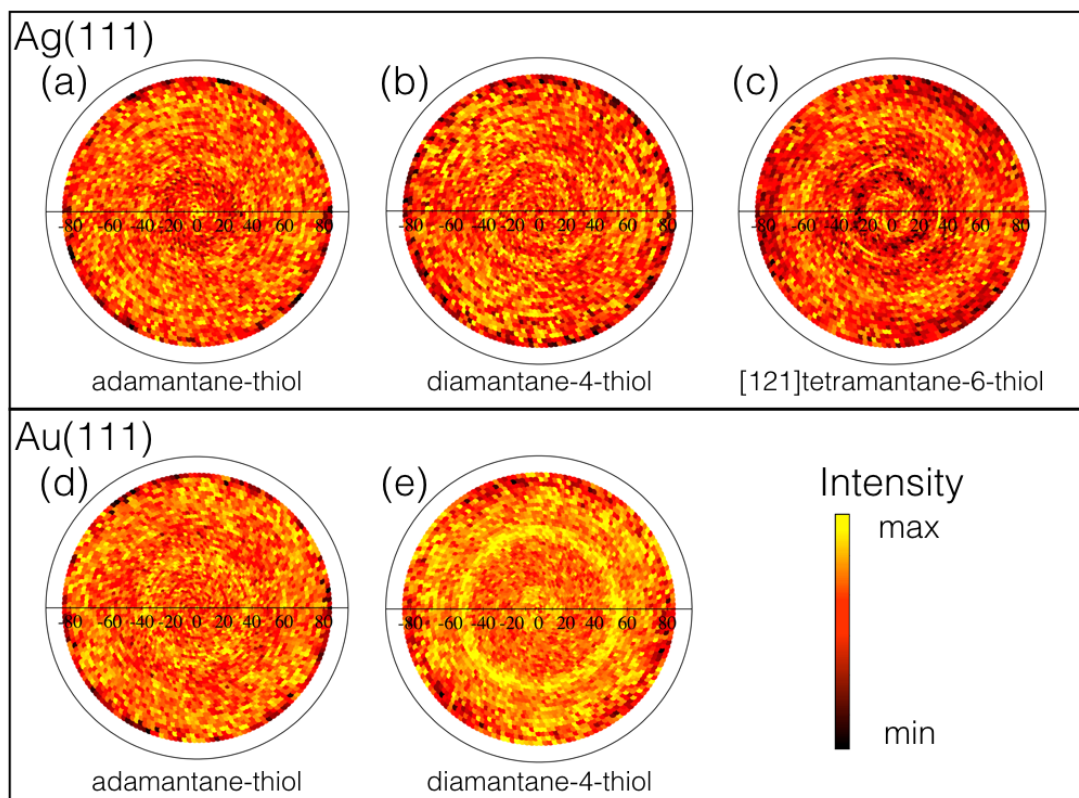


FIGURE 4.10: XPD measurements of different diamondoids on Ag(111) and Au(111) are shown, (a) adamantane-thiol/Ag(111), (b) diamantane-4-thiol/Ag(111), (c) [121]tetramantane-6-thiol/Ag(111), (d) adamantane-thiol/Au(111) and (e) diamantane-4-thiol/Au(111). All diffraction patterns show a polar range from normal emission in the center to $\Theta_{max} = 82^\circ$ at the outer border and a polar angle step size of 2° . The patterns are shown as stereographic projections. All patterns were three fold averaged and were divided by a Gaussian intensity distribution. The emitter is always the S 2p core level state. All patterns show ring structures at $\Theta \approx 38^\circ$ with exception of (e) ($\Theta \approx 53^\circ$).

Some of the patterns show multiple rings such as tetramantane/Ag(111) (Fig. 4.10 (c)). This might be due to forward scattering of next nearest carbon atoms. Figure 4.11 illustrates the supposed orientation of the diamondoid. For the sake of clarity an adamantane-thiol is depicted and the terminating hydrogen atoms are not shown. The molecular axis is defined by the direction of the S-C bond. β is the angle between the molecular axis and direction from the sulfur to a next nearest carbon atom. Assuming a S-C bond length of 1.8 Å, β is calculated to be $\sim 32^\circ$. The canted molecular axis and β would allow for a forward scattering angle at a next nearest carbon of up to $\sim 70^\circ$ and a minimal scattering angle of a few degree off from the surface normal. Rotating the molecule around the molecular axis the maximum scattering angle will be decreased. Due to the hydrogen termination of the molecules the allowed twist around the molecular axis are restricted [7]. To calculate the allowed scattering angles a more complex simulation would be needed including the steric constraints on the twisting angle around the molecular axis.

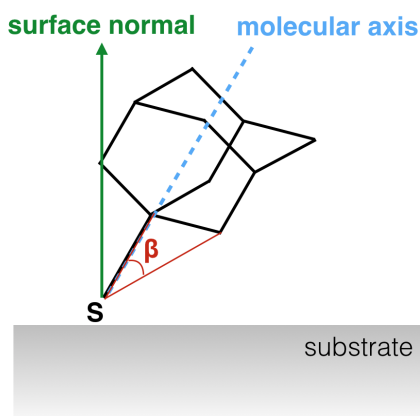


FIGURE 4.11: Illustration of the supposed orientation of adamantane-thiol, diamantane-4-thiol and [121]tetramantane-6-thiol on Ag(111)/Au(111). For the sake of clarity an adamantane-thiol with no surface hydrogen is depicted. The surface normal is shown in green. The molecular axis defined along the S-C bond is shown in blue. β is the angle between the molecular axis and the next nearest carbon atom from the sulfur.

To evaluate the positions of the rings the intensity was averaged over all azimuthal angles for every polar angle and a Gaussian was fitted to the maxima. An example for diamantane/Ag(111) is shown in Fig. 4.12. Tab. 4.3 lists the polar angles of the ring structures found in the XPD pattern. NEXAFS data from [7] indicate that the sulfur-carbon bond is tilted by $30 \pm 10^\circ$ from the surface normal for [121]tetramantane-6-thiol. Adamantane-thiol and diamantane-4-thiol adopt comparable upright orientations. Our results for the center ring are in good agreement with this. For the outer and inner rings a more rigorous discussion of the scattering angles is needed. The obtained results are within the calculated restriction for scattering at the next nearest carbon.

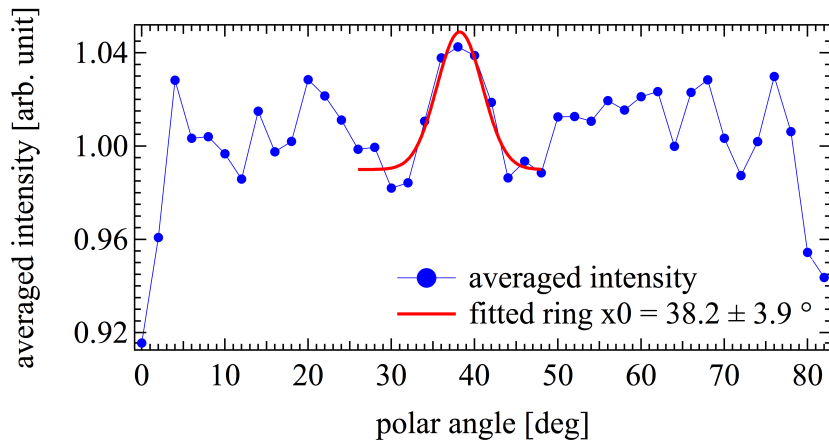


FIGURE 4.12: ϕ -averaged intensity plotted against the polar angle corresponding to the XPD 4.10 (b) (blue curve). At the supposed ring position a Gaussian was fitted to the data (red curve).

TABLE 4.3: Polar angles of ring structures from various XPD patterns of self assembled diamondoid monolayers on Ag and Au.

	inner ring [deg]	center ring [deg]	outer ring [deg]
adamantane/Ag	2.0 ± 1.8	38.8 ± 4.2	-
adamantane/Au	-	36.5 ± 6.9	-
diamantane/Ag	-	38.2 ± 3.9	-
diamantane/Au	8.2 ± 9.4	-	53.3 ± 5.3
tetramantane/Ag	13.7 ± 7.6	35.0 ± 3.1	60.5 ± 9.3

4.4 Electronic Structure

4.4.1 Ultraviolet Photoemission Experiments

Photons from the the HeI α ($h\nu = 21.22$ eV) and the HeII α ($h\nu = 40.81$ eV) gas discharge lines were primarily used to record the UPS spectra. Figure 4.13 shows a UP spectrum of a clean Ag(111) surface. The Ag 4d states, the secondary electron cutoff at 4.8 eV and the surface state are visible. Figure 4.14 shows UP spectra of different species of diamondoids on Ag(111). The spectra were normalized by setting the height of the Fermi-edge to 1, shown in the subplot. In comparison with the clean Ag(111) spectrum the 4d bands are no longer visible and a large peak at ~ 4.2 eV appears. These electrons are attributed to emission due to the negative electron affinity (NEA) of the diamondoid ad-layer. The structures between 10 eV to 15 eV could be related to the molecular orbitals of the diamondoid SAM. Table 4.4 lists the peak positions for the different UPS measurements. Figure 4.15 shows the UP spectrum of adamantane-thiol on silver (red curve) once again compared to the spectrum of the pristine silver surface (green curve). The spectrum for adamantane is shown a second time on a logarithmic scale in blue.

The assumed valence band maximum (VBM) is indicated by a vertical line. For the sake of clarity the three spectra are offset vertically.

TABLE 4.4: Peak position (LUMO) of the various combinations of diamondoid species and substrate. Data recorded using the HeI α and HeII α discharge line except otherwise stated. Energy with respect to E_F of the substrate.

	HeI α		HeII α	
	Ag(111) [eV]	Au(111) [eV]	Ag(111) [eV]	Au(111) [eV]
adamantane-thiol	4.12 \pm 0.05	4.19 \pm 0.05	4.13 \pm 0.05	4.20 \pm 0.05
diamantane-4-thiol	4.19 \pm 0.05	4.21 \pm 0.05*	4.27 \pm 0.05	4.17 \pm 0.05
[121]tetramantane-6-thiol	4.18 \pm 0.05	-	4.20 \pm 0.05	-

*recorded using HeI β

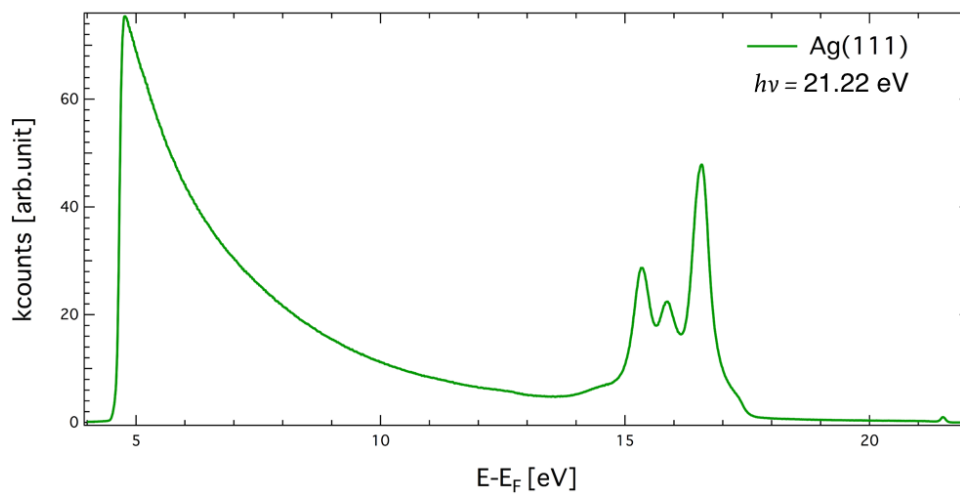


FIGURE 4.13: UP spectrum of the Ag(111) surface in normal emission plotted against the final state energy with respect to the Fermi energy. The Ag 4d states are visible between 15 eV to 17 eV. The secondary electron cutoff at 4.8 eV and the surface state are visible.

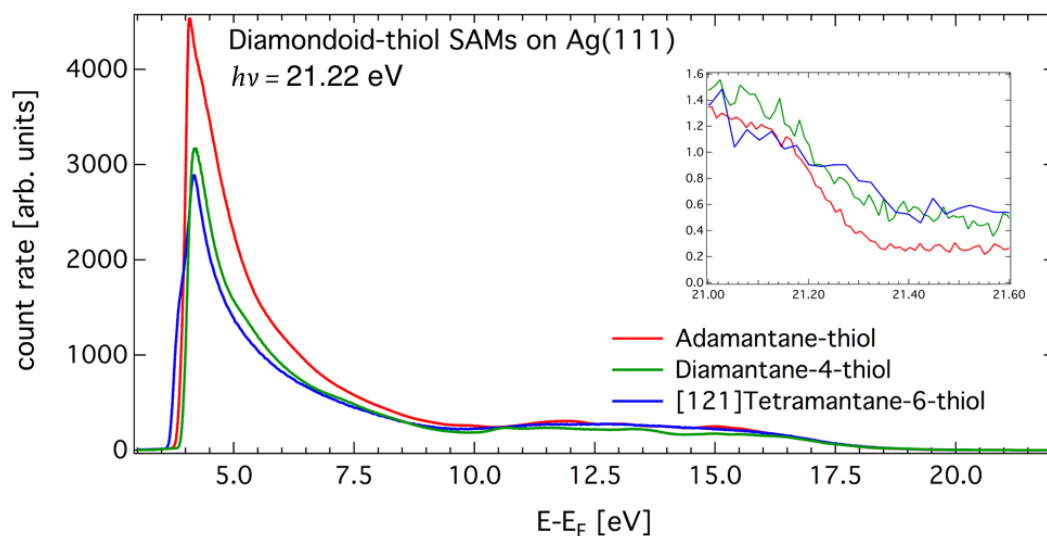


FIGURE 4.14: HeI α UP spectra for different diamondoid species on Ag(111). The large peak at ~ 4.2 eV corresponds to electrons emitted through the LUMO. The structures at 10 eV to 15 eV could be related to molecular orbitals from the diamondoid ad-layer. The data was normalized to a height of the Fermi-edge of 1. The Fermi energy is shown in the subplot on the right hand side.

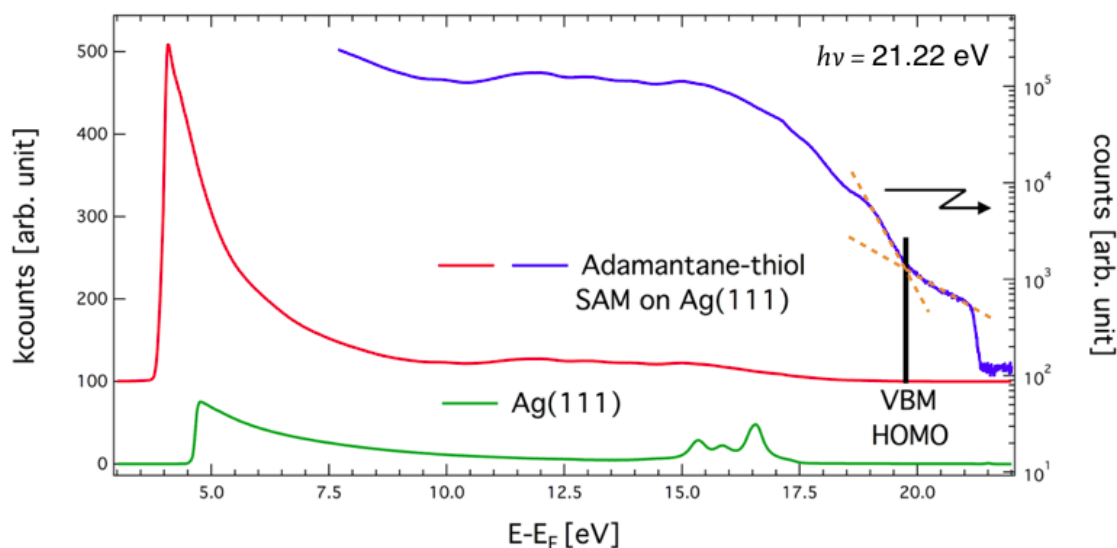


FIGURE 4.15: UP spectrum of adamantane-thiol on silver (red curve) plotted against the final state energy with respect to the Fermi energy. For direct comparison a spectrum of a clean Ag(111) surface (green curve) is shown. The spectrum for adamantane-thiol is shown a second time against a logarithmic scale (blue curve). For clarity the three spectra are offset vertically. The assumed valence band maximum (VBM) is indicated with a vertical line. The dashed orange lines were used to estimate the VBM.

The ratio of electrons emitted through the NEA peak and the total number of emitted electrons varied for different species and substrates and as a function of $h\nu$ from 41 % to 71 % see table 4.5. These values are in good agreement with the observations for [121]tetramantane-6-thiol of $\sim 35\%$ [16]. To calculate the ratio the spectrum was integrated over the NEA peak (blue area) and divided by the total yield of the spectrum (red area) see Figure 4.16

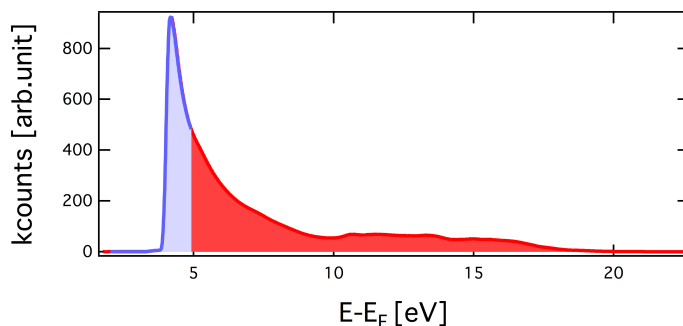


FIGURE 4.16: To calculate the ratio of electrons emitted through the LUMO and the total yield. The NEA peak was integrated up to the energy corresponding to half the maximum intensity (blue area) and divided by the total yield (red area).

TABLE 4.5: Ratio of emitted electrons from NEA peak (LUMO) and total yield for various combinations of diamondoid species and substrates. Data recorded using the HeI α and HeII α discharge line except otherwise stated.

	HeI α		HeII α	
	Ag(111)	Au(111)	Ag(111)	Au(111)
adamantane-thiol	0.707 ± 0.001	0.583 ± 0.003	0.665 ± 0.001	0.414 ± 0.002
diamantane-4-thiol	0.569 ± 0.001	$0.596 \pm 0.002^*$	0.587 ± 0.001	0.634 ± 0.002
[121]tetramantane-6-thiol	0.409 ± 0.001	-	0.483 ± 0.001	-

*recorded using HeI β

4.4.2 Two-Photon Photoemission Experiments

In order to record two-photon photoemission (2PPE) spectra photons of various energies were used (2.35 eV to 4.00 eV). A sufficient photon density was provided by the laser setup described in Section 3.1. The exact photon energy varied between different beam-times, but overall similar energies and energy-spacings were used for all preparations. In addition for every photon energy a spectrum of a clean poly-crystalline Ag surface was taken to account for differences in photon flux. All energies are given with respect to the Fermi energy of the substrate. Figure 4.17 shows 2PPE spectra for adamantane-thiol and diamantane-4-thiol on silver using wavelengths of 400 nm. The position of the NEA peak remains unchanged at ~ 4.2 eV for diamantane and ~ 4.1 eV for adamantane.

The full width at half maximum (FWHM) of the NEA peak is ~ 350 meV for both diamondoid species. An estimation of the work function will be made later.

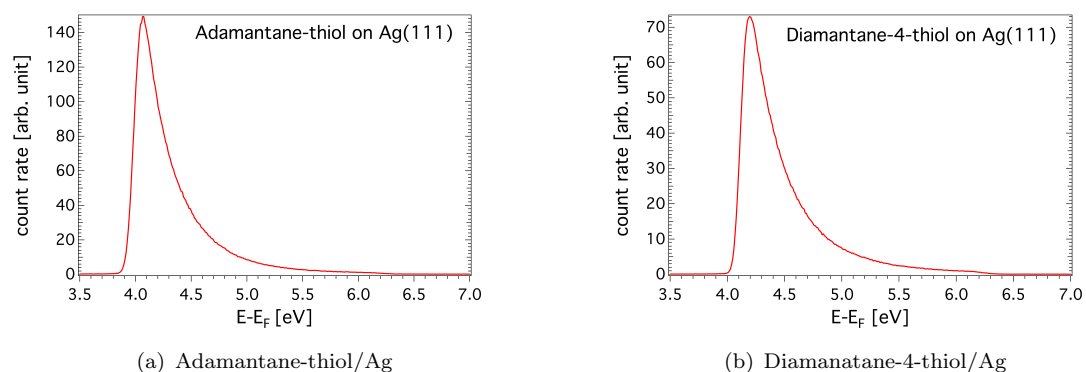


FIGURE 4.17: Two-photon photoemission spectra of adamantane-thiol and diamantane-4-thiol monolayers on Ag(111), $h\nu = 3.1$ eV (400 nm).

Figures 4.18, 4.19, 4.20, and 4.21 show 2PPE spectra of adamantane and diamantane monolayers on Ag(111) and Au(111) for different wavelengths. The data were normalized to the height of the Fermi-edge of the corresponding Ag(poly) spectra. The energy positions of the NEA peak for the four different systems are listed in Tab. 4.6.

TABLE 4.6: NEA peak position for adamantane and diamantane on Ag(111) and Au(111) with respect to E_F .

	Ag(111) [eV]	Au(111)[eV]
adamantane-thiol	4.08 ± 0.03	4.14 ± 0.03
diamantane-4-thiol	4.17 ± 0.02	4.19 ± 0.04

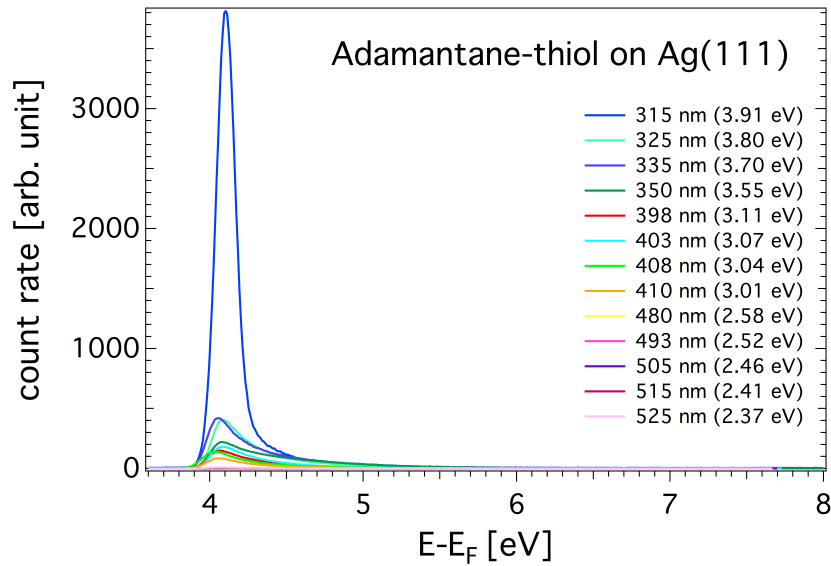


FIGURE 4.18: 2PPE spectra from an adamantane monolayer on Ag(111) taken with various photon energies. The color chart denotes the wavelengths in nanometers, in brackets the corresponding photon energies are given. The spectra above 398 nm were taken with the frequency doubled OPA output. For the spectra between 398 nm to 413 nm the Mira beam was frequency doubled. For wavelengths ≥ 480 nm the OPA output was used. The data were normalized to the height of the Fermi-edge of a corresponding Ag(poly) spectrum to account for different photon fluxes.

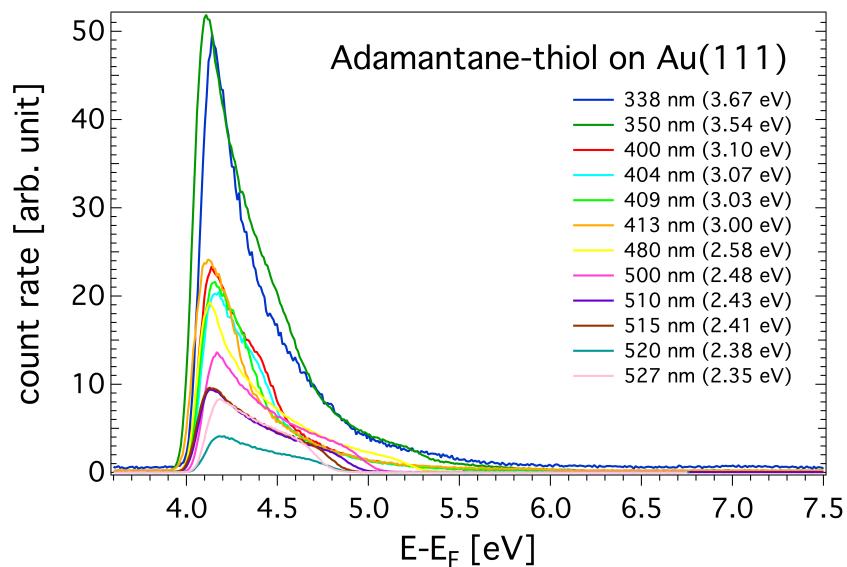


FIGURE 4.19: As in Figure 4.18: 2PPE spectra from an adamantane monolayer on Au(111) taken with various photon energies.

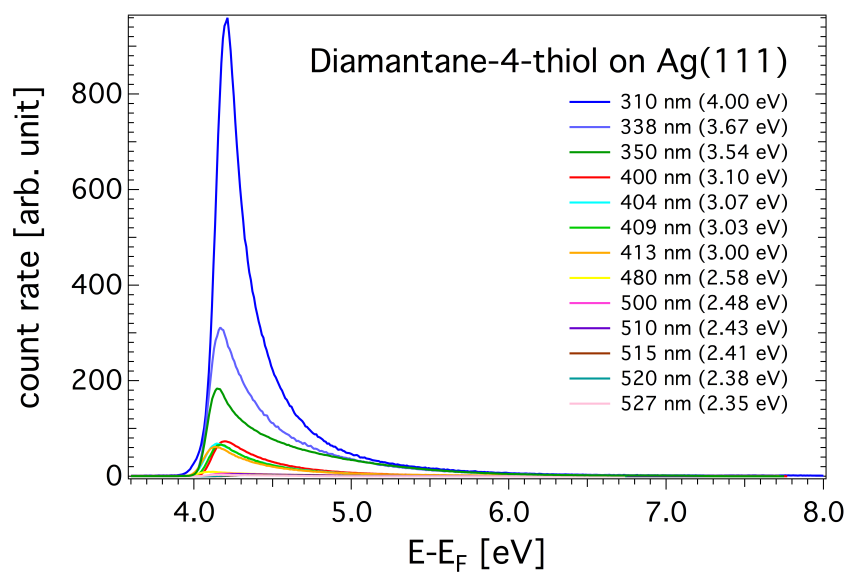


FIGURE 4.20: As in Figure 4.18: 2PPE spectra from a diamantane monolayer on Ag(111) taken with various photon energies.

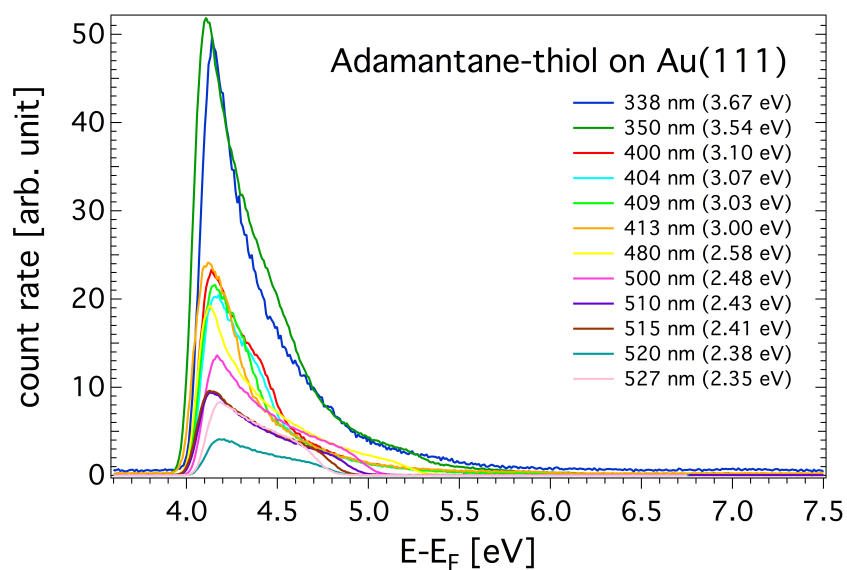


FIGURE 4.21: As in Figure 4.18: 2PPE spectra from a diamantane monolayer on Au(111) taken with various photon energies.

The intensity of the NEA peak decreases for larger wavelengths. Overall a smaller intensity is observed for diamondoid monolayers on Au(111) than from the same diamondoid on Ag(111). This seems reasonable if we take into account that ratio of surface atoms to molecules for gold is 5.7 compared to 3 on silver.

Electron emitted from E_F appear in a 2PPE spectrum at $E - E_F = 2h\nu$. The Fermi-edge moves with twice the photon energy. Figure 4.22 shows the position of the Fermi-edge as a function of photon energy for different lower diamondoids on Ag and Au. The Fermi-edge follows a line with slope $m = 2$.

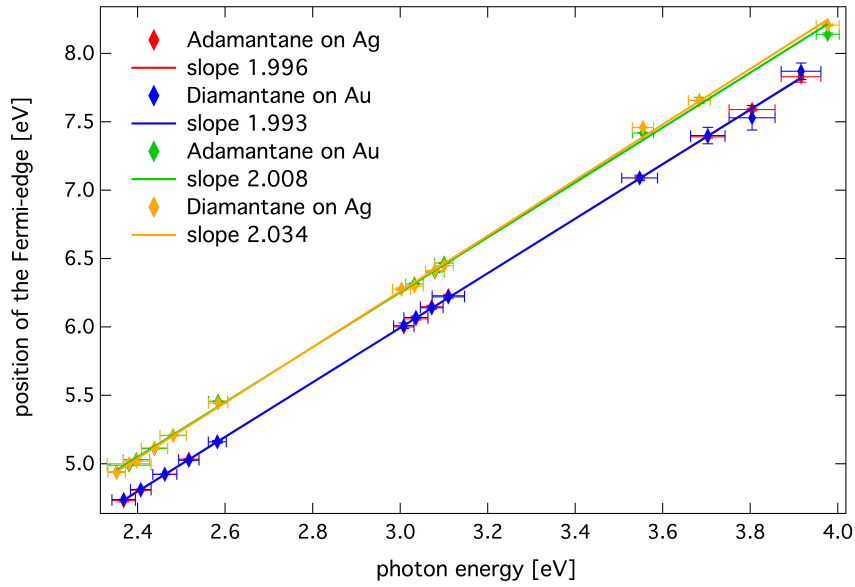


FIGURE 4.22: The position of the Fermi-edge for adamantane and diamantane on Ag and Au is plotted against the photon energy. The fitted lines all have a slope $m = 2$.

Since the position of the NEA peak is independent of $h\nu$ (see Fig. 4.23) this is no indication of a two photon process. The intensity of a two photon process is proportional to the square of the light intensity:

$$I_{NEA} \propto I_{light}^2. \quad (4.10)$$

Hence the logarithm of the NEA intensity vs the logarithm of the intensity of the light should follow a line with slope $m = 2$. Figure 4.24 shows the logarithm of the NEA intensity vs the logarithm of the laser power for diamantane-4-thiol on silver and $\lambda = 480$ nm. The slope $m = 2.3$ indicates a two photon process with an considerable amount of three photon processes. This is probably due to the small photon energy.

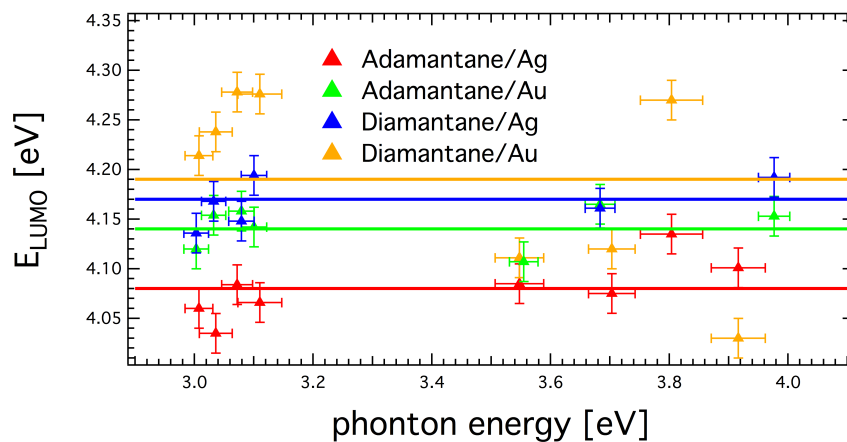


FIGURE 4.23: LUMO energy plotted against photon energy. The LUMO energy listed in table 4.6 is indicated by a solid line. The position of the LUMO is reasonably constant for all photon energies.

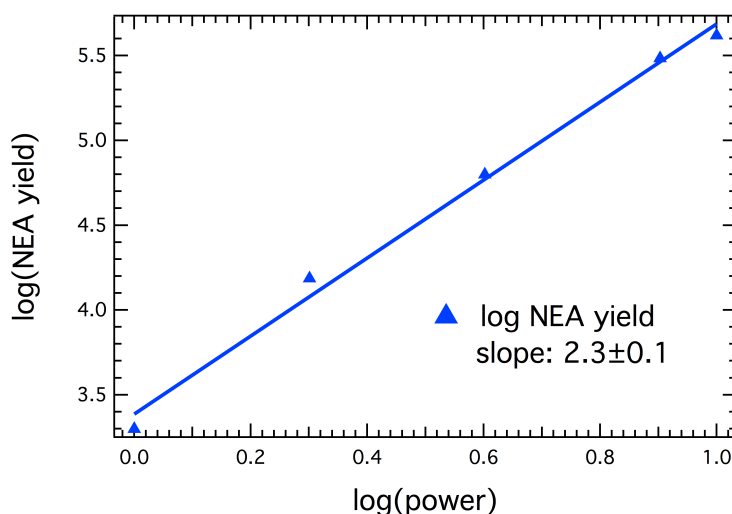


FIGURE 4.24: Logarithm of the electron yield from NEA to logarithm of the laser power. The slope of 2.3 indicates a two photon process with a considerable amount of three photon processes.

Figure 4.25 compares the ratio of electrons emitted via the LUMO and the total electron yield of different diamondoids and for UPS and 2PPE measurements. The ratio seems to decrease for increasing number of cages, except for the 2PPE data from Ag(111) which show a slight increase. Note that the UPS spectrum for two (diamantane) on gold is not directly comparable since it was recorded using the $\text{He}1\beta$ discharge line. These data are shown for the sake of completeness.

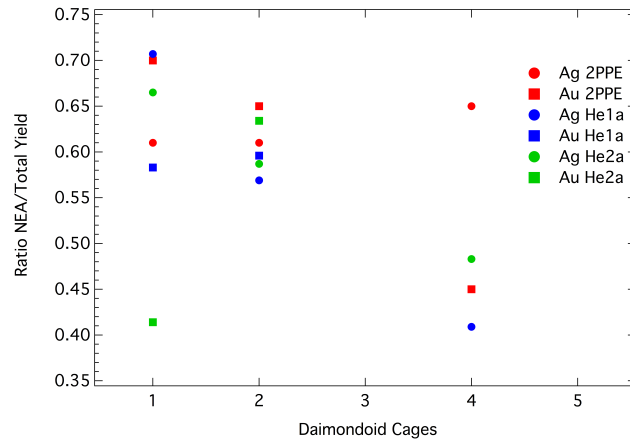


FIGURE 4.25: The ratio of electrons emitted through the LUMO to total electron yield is shown against the diamondoid cage number. Note adamantane has one cage, diamantane is built by two cages and tetramantane consists of four cages. Note the spectrum for 2 (diamantane) on Au(111) was taken using the He1 β discharge line and is shown for the sake of completeness. 2PPE data for 4 (tetramantane) were taken from [16].

In Ref. [20] a threshold behavior for the emission of electrons through the LUMO was observed for [121]tetramantane-6-thiol SAM on Ag(111) and Au(111). An total photon energy of 5.56 ± 0.04 eV on Ag and 5.74 ± 0.04 eV on Au was found to excite electrons from the conduction band into a final state at the same or a higher energy than the LUMO. The results from [20] are shown in Figure 4.26.

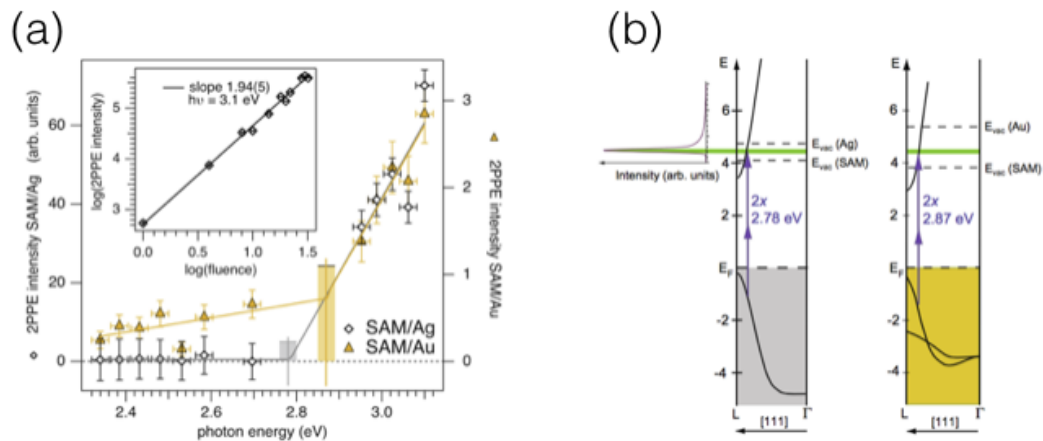


FIGURE 4.26: Threshold energy for [121]tetramantane-6-thiol taken from [20]. (a) Photon energy dependence of the NEA peak intensity in 2PPE spectra. The extrapolated photon energy thresholds are marked by rectangles in both cases, the widths denote the uncertainty. (b) Threshold transition in the substrate band structure. The substrate band structure is shown along the (111)-direction. The threshold transitions into the LUMO (green line) are indicated by blue arrows.

Using the same method we investigated if adamantane and diamantane show a similar threshold behavior. Figure 4.27 shows the peak intensity of the NEA peak plotted versus the photon energy. The spectra were normalized carefully to the height of the corresponding spectrum of a poly-crystalline Ag sample. For both diamondoid species no threshold behavior was observed on gold. On silver the extrapolated intensity indicates a threshold photon energy of $h\nu = 2.69 \pm 0.1$ eV for adamantane and $h\nu = 2.91 \pm 0.1$ eV for diamantane. The threshold energy is twice this energy $E_{ada/th} = 5.38 \pm 0.2$ eV and $E_{dia/th} = 5.82 \pm 0.2$ eV. As with tetramantane one can compare this result with the band structure. We find that those energies will excite electrons inside the substrate to an energy above the LUMO of the molecule. The band structure and the transitions are shown in Figure 4.28. The energy difference of the final state inside the substrate and the LUMO is ~ 0.5 eV. Due to the steep slope of the involved bands a shift or error in the LUMO position of $\Delta E_{LUMO} = 0.1$ eV results in a change of the threshold energy of $\Delta E_{threshold} = 0.2$ eV. After excitation inside the substrate the excited electron is transferred to the molecule where it relaxes to the LUMO and is emitted. The comparably short inelastic mean free path found by [21] might support such a strong relaxation process inside the molecule.

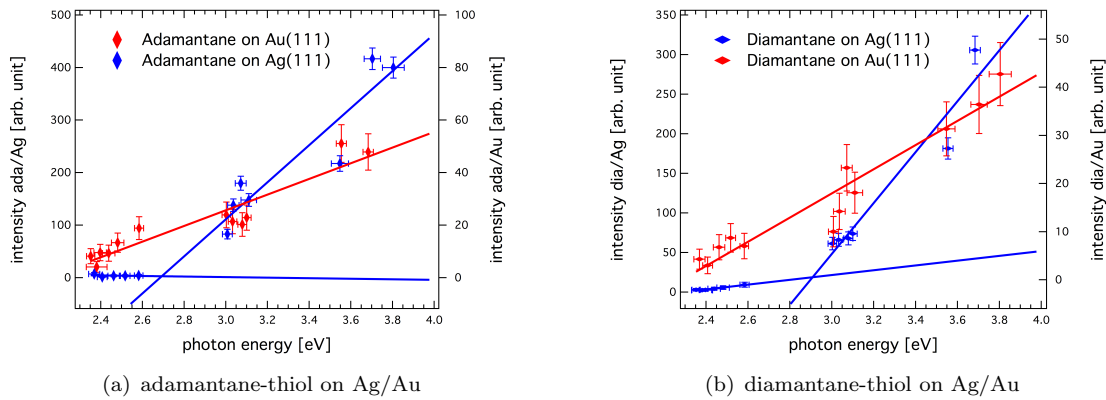
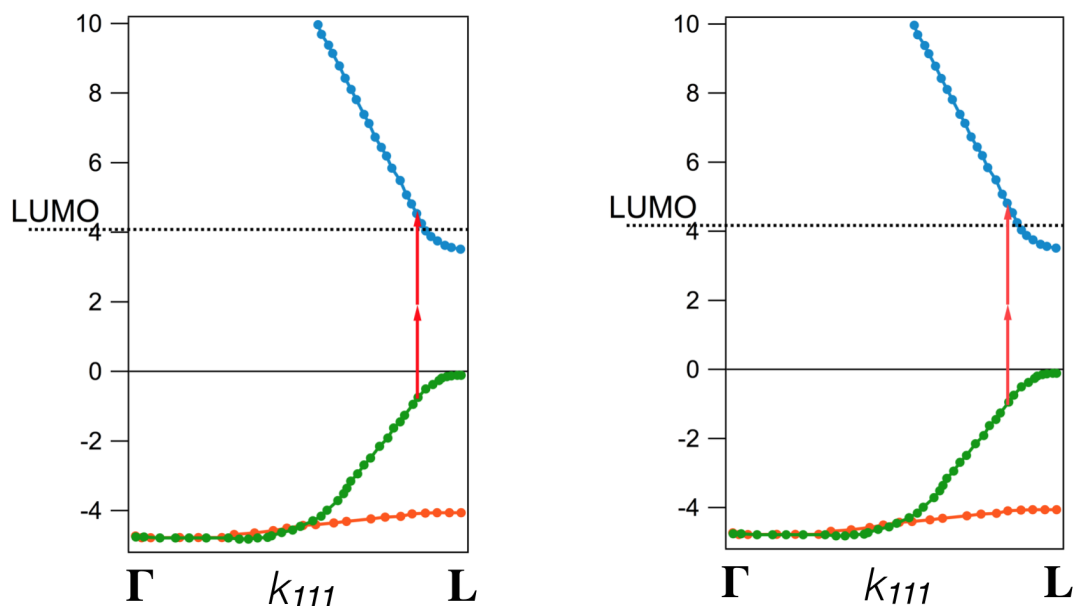


FIGURE 4.27: Photon energy dependence of the NEA peak intensity. **(a)** Data for adamantane/Ag shown in blue. A threshold photon energy of $h\nu = 2.69 \pm 0.1$ eV is obtained by extrapolating the intensity for energy below and above this threshold. For adamantane/Au all data point fit a line and no threshold energy could be obtained. **(b)** As in (a) for diamantane-4-thiol. A threshold energy on Ag of $h\nu = 2.91 \pm 0.1$ eV was obtained.



(a) adamantane-thiol LUMO position in Ag(111) band structure

(b) diamantane-4-thiol LUMO position in Ag(111) band structure

FIGURE 4.28: Threshold transitions in the Ag band structure. The band structure in both panels is shown along the [111]-direction from Γ to L . The LUMO position of the diamondoid is depicted by a dashed black line. Both transitions with twice the found photon energy lead to final states ~ 0.5 eV above the LUMO. Substrate band structure taken from Ref. [22].

4.4.3 Work function and HOMO-LUMO Gap

An estimation of the work function can be made by calculating the change of the substrate work function due to the dipole moment of the thiol bond. Calculations of the work function change for alkanethiols on Ag and Au can be found in [23]. The work function shift can be estimated as follows:

$$\Delta\Phi = \frac{\Delta\mu e}{\epsilon_0 A} \quad (4.11)$$

if only molecular dipoles are taken into account. Here $\Delta\mu$ is the dipole per molecule, e the charge of an electron, ϵ_0 the vacuum permittivity and A the area of the surface unit cell corresponding to one molecule. The values used for the calculations are listed in Tab. 4.7. Since the underived diamondoid has no dipole moment the dipole moment of the thiolated diamondoid was approximated the dipole moment of the M-S-C bond of M-S-CH₃, taken from Ref.[23]. The area of the surface unit cell was calculated from XPS data.

Tab. 4.8 lists the estimated work functions and electron affinities. For adamantane-thiol a decrease of $\Delta\Phi = 0.67$ eV on silver and $\Delta\Phi = 0.77$ eV on gold is estimated, resulting

TABLE 4.7: Dipole moment of M-S-CH₃, work function Φ of pristine surfaces and area of the surface unit cell A for Ag and Au. Dipole moment taken from Ref. [23].

	Ag(111)	Au(111)
$\Delta\mu$ [D]	-0.32	-0.86
Φ [eV]	4.74	5.31
A_{ada} [\AA^2]	18.07	42.32
A_{dia} [\AA^2]	20.45	43.21

TABLE 4.8: Estimated work function and electron affinity of diamondoid monolayers.

	Ag(111)	Au(111)
Φ_{ada} [eV]	4.07	4.54
Φ_{dia} [eV]	4.15	4.56
E_{EAada} [eV]	-0.01	0.42
E_{EAadia} [eV]	-0.02	0.37

in an estimated work function for the adamantane monolayer of $\Phi_{ada/Ag} = 4.07$ eV and $\Phi_{ada/Au} = 4.54$ eV, respectively. For diamantane we find an estimated reduction of the work function of $\Delta\Phi = 0.59$ eV on silver and $\Delta\Phi = 0.75$ eV on gold. Therefore, the estimated work function of diamantane monolayer are $\Phi_{dia/Ag} = 4.15$ eV and $\Phi_{dia/Au} = 4.56$ eV. With this we estimate the electron affinity for adamantane to be $E_{EA} = 0.42$ eV on gold and $E_{EA} = -0.01$ eV on silver. For diamantane-4-thiol electron affinities are estimated to $E_{EA} = 0.37$ eV on gold and $E_{EA} = -0.02$ eV on silver respectively. This would mean there is no negative electron affinity on gold and the peak on silver is not distinguishable from the secondary electron cutoff. For the diamondoids on gold we clearly have signal below the estimated work function which puts the proposed model, for estimating the work function, in question. DFT calculations by Narashimha et al. estimate a workfunction for adamanatane/Au, diamantane/Au, and tetramantane/Au of ~ 4.2 eV [24]. In addition to the intrinsic dipole moment, the chemisorption dipole, and the 'cushion effect', which arises from repulsion between the surface and molecular electron orbitals were taken into account. Taking these into account comparable results might be obtained in our case.

Density functional computations for [121]tetramante-6-thiol were preformed by Fokin and Schreiner and the result are shown in reference [20]. Figure 4.29 shows the resulting HOMO and LUMO positions for [121]tetramante-6-thiol calculated with the GAUSSIAN 03 program suite. Both orbitals are located around the sulfur atom. A HOMO-LUMO gap of 6.9 eV was obtained for [121]tetramante-6-thiol in gas phase [20]. Due to the positions of the HOMO and the LUMO one can expect similar HOMO-LUMO gaps for all rod like configurations of diamondoids with the thiol group at an end position.

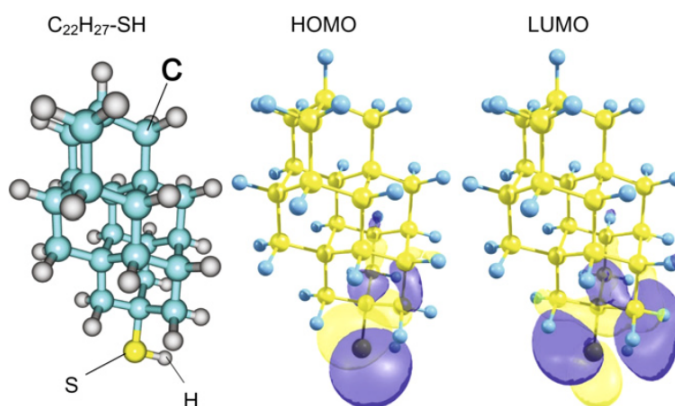


FIGURE 4.29: Molecular orbitals of [121]tetramante-6-thiol. **Left hand side:** Ball and stick model of [121]tetramante-6.thiol terminated by hydrogen. **Center:** Highest occupied molecular orbital (HOMO). **Right hand side:** Lowest unoccupied molecular orbital (LUMO). For the sake of clarity the atom positions were superimposed. Taken from Ref.[20].

Using the estimated valence band maxima (VBM) from the UPS experiments (for an example see Figure 4.15) and the LUMO positions from Table 4.6 we can estimate the HOMO-LUMO gap. For adamantane-thiol we estimate the HOMO-LUMO gap to be 5.75 ± 0.17 eV and 5.68 ± 0.15 eV for diamantane-4-thiol. This is comparable with the result for [121]tetramante-6-thiol of $5.7_{-0}^{+0.2}$ eV [20]. This is a reasonable assumption as HOMO and LUMO are located at the sulfur atom.

Chapter 5

Conclusion

Self-assembled monolayers of adamantane and diamantane were grown on Ag(111) and Au(111) surfaces. XPS data of the S 2p_{3/2} binding energy show that the diamondoid molecules are bound by a metal thiol bond to the surface. The data allow to determine a coverage of one monolayer for all diamondoid substrate combinations (1 diamondoid molecule per 3 silver atoms and 5.7 gold atoms).

XPD data taken with the S 2p_{3/2} state as emitter show ring structures at a polar angle $\theta \approx 38^\circ$. Those correspond to the forward scattering along the sulfur carbon bond which is in good agreement with results from other groups. Some patterns show ring structures at polar angles $\leq 15^\circ$ and between 53° to 60.5° which we propose to correspond to scattering at the next nearest carbon atom.

Ultraviolet photoelectron spectroscopy and two-photon photoemission experiments were carried out to determine the electronic structure of the system. UPS spectra were recorded using the HeI α ($h\nu = 21.22$ eV) and the HeII α ($h\nu = 40.81$ eV) gas discharge lines. The 2PPE experiments used photon energies from 2.35 eV to 4.00 eV.

The LUMO position was found to be ~ 4.1 eV for adamantane and ~ 4.2 eV for diamantane above the Fermi-edge of the substrate. The HOMO-LUMO gap of ~ 5.7 eV for SAM of both investigated diamondoid species is comparable to the HOMO-LUMO gap of a SAM of [121]tetramantane-6-thiol. This is reasonable taking into account the position of the HOMO and LUMO which both are located at the sulfur.

A threshold like behavior for electrons emitted through the LUMO was observed for adamantane and diamantane on silver. The threshold energy can be related to a transition inside the silver band structure. Due to the energy difference of the transition and the LUMO we propose a relaxation of the electron inside the molecule from which it is emitted due to negative electron affinity.

The work functions were estimated to be $\Phi_{ada/Ag} = 4.07$ eV and $\Phi_{ada/Au} = 4.54$ eV for adamantane and $\Phi_{dia/Ag} = 4.15$ eV and $\Phi_{dia/Au} = 4.56$ eV. With this we estimate the

electron affinity for adamantane to be $E_{EA} = 0.42$ eV on gold and $E_{EA} = -0.01$ eV on silver. For diamantane-4-thiol electron affinities are estimated to $E_{EA} = 0.37$ eV on gold and $E_{EA} = -0.02$ eV on silver respectively. Electrons were measured well below the estimated work function of diamondoid SAM on gold. This puts the proposed model for estimating the work function in question. By including the chemisorption dipole and the 'cushion effect' better results might be obtained.

Understanding the reason for the differences in the threshold behavior for adamantane, diamantane and [121]tetramantane on gold, expanding the model for estimating the work function as described above, and verifying the origins of the ring structure in the XPD by simulation and calculation of the allowed scattering angles including the steric constraints might be interesting topics for future work.

Bibliography

- [1] W A Clay, J E P Dahl, R M K Carlson, N A Melosh, and Z-X Shen. Physical properties of materials derived from diamondoid molecules. *Reports on Progress in Physics*, 78(1):016501, 2015. URL <http://stacks.iop.org/0034-4885/78/i=1/a=016501>.
- [2] S. Landa and V. Machacek. *Coll. Czech. Chem. Commun.* 5, 1 1933.
- [3] J. E. Dahl, S. G. Liu, and R. M. K. Carlson. Isolation and structure of higher diamondoids, nanometer-sized diamond molecules. *Science*, 299(5603):96–99, 2003.
- [4] W. L. Yang, J. D. Fabbri, T. M. Willey, J. R. I. Lee, J. E. Dahl, R. M. K. Carlson, P. R. Schreiner, A. A. Fokin, B. A. Tkachenko, N. A. Fokina, W. Meevasana, N. Mannella, K. Tanaka, X. J. Zhou, T. van Buuren, M. A. Kelly, Z. Hussain, N. A. Melosh, and Z.-X. Shen. Monochromatic electron photoemission from diamondoid monolayers. *Science*, 316(5830):1460–1462, 2007.
- [5] C. Bandis and B. B. Pate. Electron emission due to exciton breakup from negative electron affinity diamond. *Phys. Rev. Lett.*, 74:777–780, Jan 1995.
- [6] J. C. Gröbli, D. Guarisco, S. Frank, and F. Meier. Spin-dependent transmission of polarized electrons through a ferromagnetic iron film. *Phys. Rev. Lett.*, 51:2945–2949, Feb 1995.
- [7] Trevor M. Willey, Jason D. Fabbri, Jonathan R. I. Lee, Peter R. Schreiner, Andrey A. Fokin, Boryslav A. Tkachenko, Nataliya A. Fokina, Jeremy E. P. Dahl, Robert M. K. Carlson, Andrew L. Vance, Wanli Yang, Louis J. Terminello, Tony van Buuren, and Nicolas A. Melosh. Near-edge x-ray absorption fine structure spectroscopy of diamondoid thiol monolayers on gold. *Journal of the American Chemical Society*, 130(32):10536–10544, 2008.
- [8] A. Einstein. Ueber einen die Erzeugung und Verwandlung des Lichtes betreffenden heuristischen Gesichtspunkt. *Annalen der Physik*, 322:132–148, 1905.

- [9] C. Nordling K. Siegbahn. Esca, atomic, molecular and solid state structure studies by means of electron spectroscopy. *Nova Acta Regiae Soc. Sci., Upsaliensies, Ser. IV.*, 20, 1967.
- [10] Jürg Osterwalder. *Electron Based Methods: 3.2.2 Photoelectron Spectroscopy and Diffraction*, pages 151–214. Wiley-VCH Verlag GmbH & Co. KGaA, 2014. ISBN 9783527680535.
- [11] H. C. Poon and S. Y. Tong. Focusing and diffraction effects in angle-resolved x-ray photoelectron spectroscopy. *Phys. Rev. B*, 30:6211–6213, Nov 1984. doi: 10.1103/PhysRevB.30.6211. URL <http://link.aps.org/doi/10.1103/PhysRevB.30.6211>.
- [12] Michael Greif. *Time-Resolved Photoelectron Diffraction*. PhD thesis, University of Zurich, 2015.
- [13] Hans-Joachim Eichler und Heinrich Gobrecht. *Lehrbuch der Experimentalphysik, Band 3 Optik*. De Gruyter, 1987.
- [14] Coherent Inc. *Optical Parametric Amplifier Operator’s Manual*.
- [15] T. Greber, O. Raetz, T. J. Kreutz, P. Schwaller, W. Deichmann, E. Wetli, and J. Osterwalder. A photoelectron spectrometer for k-space mapping above the Fermi level. *Review of Scientific Instruments*, 68:4549–4554, 1997.
- [16] Silvan Roth. Two-photon photoemission from tetramantane monolayers. Master Thesis, University of Zurich, 8 2008.
- [17] Rodrigo M Petoral Jr. and Kajsa Uvdal. {XPS} and {NEXAFS} study of tyrosine-terminated propanethiol assembled on gold. *Journal of Electron Spectroscopy and Related Phenomena*, 128(2–3):159 – 164, 2003.
- [18] J.J. Yeh and I. Lindau. Atomic subshell photoionization cross sections and asymmetry parameters: $1 \leq z \leq 103$. *Atomic Data and Nuclear Data Tables*, 32(1):1 – 155, 1985. doi: [http://dx.doi.org/10.1016/0092-640X\(85\)90016-6](http://dx.doi.org/10.1016/0092-640X(85)90016-6).
- [19] Jason Christopher Randel. *Quantum imaging and spectroscopy of molecular diamondoids and topological nanostructures*. PhD thesis, Stanford University, 2011.
- [20] S. Roth, D. Leuenberger, J. Osterwalder, J.E. Dahl, R.M.K. Carlson, B.A. Tkachenko, A.A. Fokin, P.R. Schreiner, and M. Hengsberger. Negative-electron-affinity diamondoid monolayers as high-brilliance source for ultrashort electron pulses. *Chemical Physics Letters*, 495(1–3):102 – 108, 2010.

-
- [21] William A. Clay, Zhi Liu, Wanli Yang, Jason D. Fabbri, Jeremy E. Dahl, Robert M. K. Carlson, Yun Sun, Peter R. Schreiner, Andrey A. Fokin, Boryslav A. Tkachenko, Nataliya A. Fokina, Piero A. Pianetta, Nicholas Melosh, and Zhi-Xun Shen. Origin of the monochromatic photoemission peak in diamondoid monolayers. *Nano Letters*, 9(1):57–61, 2009. doi: 10.1021/nl802310k. URL <http://dx.doi.org/10.1021/nl802310k>.
- [22] H Eckardt, L Fritsche, and J Noffke. Self-consistent relativistic band structure of the noble metals. *Journal of Physics F: Metal Physics*, 14(1):97, 1984.
- [23] Paul C. Rusu and Geert Brocks. Work functions of self-assembled monolayers on metal surfaces by first-principles calculations. *Phys. Rev. B*, 74:073414, Aug 2006. doi: 10.1103/PhysRevB.74.073414. URL <http://link.aps.org/doi/10.1103/PhysRevB.74.073414>.
- [24] Karthik Thimmavajjula Narasimha, Chenhao Ge, Jason D. Fabbri, William Clay, Boryslav A. Tkachenko, Andrey A. Fokin, Peter R. Schreiner, Jeremy E. Dahl, Robert M. K. Carlson, ShenZ. X., and Nicholas A. Melosh. Ultralow effective work function surfaces using diamondoid monolayers. *Nat Nano*, 11(3):267–272, 03 2016.